

GPUMD: A package for constructing accurate machine-learned potentials and performing highly efficient atomistic simulations

Zheyong Fan,^{1, a)} Yanzhou Wang,^{2,3} Penghua Ying,⁴ Keke Song,³ Junjie Wang,⁵ Yong Wang,⁵ Zezhu Zeng,⁶ Ke Xu,⁷ Eric Lindgren,⁸ J. Magnus Rahm,⁸ Alexander J. Gabourie,⁹ Jiahui Liu,³ Haikuan Dong,^{1,3} Jianyang Wu,⁷ Yue Chen,⁶ Zheng Zhong,⁴ Jian Sun,^{5, b)} Paul Erhart,^{8, c)} Yanjing Su,^{3, d)} and Tapio Ala-Nissila^{2, 10}

¹⁾College of Physical Science and Technology, Bohai University, Jinzhou 121013, P. R. China

²⁾MSP group, QTF Centre of Excellence, Department of Applied Physics, Aalto University, FI-00076 Aalto, Espoo, Finland

³⁾Beijing Advanced Innovation Center for Materials Genome Engineering, University of Science and Technology Beijing, Beijing 100083, China

⁴⁾School of Science, Harbin Institute of Technology, Shenzhen, 518055, P. R. China

⁵⁾National Laboratory of Solid State Microstructures, School of Physics and Collaborative Innovation Center of Advanced Microstructures, Nanjing University, Nanjing 210093, China

⁶⁾Department of Mechanical Engineering, The University of Hong Kong, Pokfulam Road, Hong Kong SAR, China

⁷⁾Department of Physics, Research Institute for Biomimetics and Soft Matter, Jiujiang Research Institute and Fujian Provincial Key Laboratory for Soft Functional Materials Research, Xiamen University, Xiamen 361005, PR China

⁸⁾Chalmers University of Technology, Department of Physics, 41926 Gothenburg, Sweden

⁹⁾Department of Electrical Engineering, Stanford University, Stanford, California 94305, USA

¹⁰⁾Interdisciplinary Centre for Mathematical Modelling, Department of Mathematical Sciences, Loughborough University, Loughborough, Leicestershire LE11 3TU, UK

(Dated: 23 May 2022)

We present our latest advancements of machine-learned potentials (MLPs) based on the neuroevolution potential (NEP) framework introduced in [Fan *et al.*, Phys. Rev. B **104**, 104309 (2021)] and their implementation in the open-source package GPUMD. We increase the accuracy of NEP models both by improving the radial functions in the atomic-environment descriptor using a linear combination of Chebyshev basis functions and by extending the angular descriptor with some four-body and five-body contributions as in the atomic cluster expansion approach. We also detail our efficient implementation of the NEP approach in graphics processing units as well as our workflow for the construction of NEP models, and we demonstrate their application in large-scale atomistic simulations. By comparing to state-of-the-art MLPs, we show that the NEP approach not only achieves above-average accuracy but also is far more computationally efficient. These results demonstrate that the GPUMD package is a promising tool for solving challenging problems requiring highly accurate, large-scale atomistic simulations. To enable the construction of MLPs using a minimal training set, we propose an active-learning scheme based on the latent space of a pre-trained NEP model. Finally, we introduce two separate Python packages, GPYUMD and CALORINE, which enable the integration of GPUMD into Python workflows.

I. INTRODUCTION

Machine-learned classical potentials^{1–7} have shown great promise in enabling accurate atomistic simulations far beyond the space and time scales that can be achieved using quantum mechanical calculations. Many open-source computer packages for machine-

learned potentials (MLPs) have been published, including QUIP-GAP,^{8–10} SNAP,¹¹ AMP,¹² AENET,^{13,14} ANI,¹⁵ SCHNET,¹⁶ DEEPM-D-KIT,^{17–19} TENSORMOL,²⁰ PHYSNET,²¹ MEGNET,²² TURBOGAP,²³ SGDML,²⁴ N2P2,²⁵ SIMPLE-NN,²⁶ PANNA,²⁷ FCHL,²⁸ PINN,²⁹ MLIP,^{30,31} RE-ANN,³² TABGAP,³³ PYXTAL-FF,³⁴ PYTHON-ACE,^{35,36} and KLIFF.³⁷ However, most existing implementations of MLPs (TABGAP³³ is a notable exception) have a computational speed of about 1×10^3 atom step/s using one typical CPU core, which is about two to three orders of magnitude slower than typical empirical potentials such as the Tersoff potential.³⁸ Therefore, even though MLPs are already faster than quantum-mechanical methods, it is still desirable to speed up MLPs as much as possible.

^{a)}Electronic mail: brucenju@gmail.com

^{b)}Electronic mail: jiansun@nju.edu.cn

^{c)}Electronic mail: erhart@chalmers.se

^{d)}Electronic mail: yjsu@ustb.edu.cn

One approach to speed up MLPs is to use a huge number of CPUs and/or GPUs through message-passing information parallelisation. For example, using 27,360 V100 GPUs and the same number of CPU cores, the deep potential (DP) approach^{17–19} has been used to simulate a 127-million-atom aluminum system with a speed of about 1.23×10^9 atom step/s.³⁹ However, such huge amounts of computational resources are not available to most researchers. More importantly, the performance of DP per V100 GPU is only about 4.5×10^4 atom step/s, which is about ten times *slower* than an empirical embedded atom method (EAM) potential⁴⁰ with a single typical CPU core.

A more economical approach is to optimize the formulation and implementation of the MLP itself so that it can attain a high computational speed using a reasonable amount of computational resources available to most researchers. To this end, we have developed a MLP called neuroevolution potential (NEP)^{41,42} within the GPUMD package^{43,44} that can achieve a computational speed of about 1×10^7 atom step/s using a single V100 GPU, which is about ten times *faster* than the empirical Tersoff potential on a single typical CPU core.

In this paper, we present recent developments of the NEP approach that further improve its accuracy without reducing the efficiency. Specifically, we improve the radial functions in the atomic-environment descriptor by using a combination of basis functions, and add angular descriptor components with high-order correlations. The improved radial functions are better at distinguishing different atom types and lead to higher accuracy in multi-components systems. The added angular descriptor components with high-order correlations make the atomic-environment descriptor more complete and help to increase the regression accuracy.

Using a number of systems, including MgAlCu alloy, silicon with various phases, the azobenzene molecule, and carbon with various phases, we demonstrate the accuracy and efficiency of the latest NEP as implemented in the GPUMD package. We compare with other state-of-the-art MLPs, including DP,^{17–19} Gaussian approximation potential (GAP),⁸ momentum tensor potential (MTP),^{30,31} recursive embedded-atom neural network (REANN),^{32,45} and atomic cluster expansion (ACE).^{46–48} Through these comprehensive comparisons, we show that the NEP implementation in GPUMD can achieve a computational speed that is far superior to other MLPs, under the condition of achieving an above-average accuracy. We present the algorithms for the efficient GPU implementation of NEP in great detail. Using a single GPU, such as an A100, one can use GPUMD to simulate up to 10 million atoms on nanosecond time scales, which can only be achieved by using a huge amount of computational resources with other codes. The GPUMD package makes large-scale, high-accuracy atomistic simulations available to a wide community instead of only a small number of institutions. In addition to these high-efficiency atomistic simulations, we also propose an effective active-learning

scheme based on the latent space of the NEP model that can greatly reduce the computational burden of preparing training data.

Finally, we introduce the workflow for constructing and using NEPs through concrete examples in atomistic simulations of various materials properties, including lattice constant, elastic constants, stress-strain relation during tensile loading, structural properties during a melt-quench-anneal process, and thermal properties of amorphous structures. We also describe interfacing GPUMD to Python via the GPYMD and CALORINE packages.

II. THEORETICAL FORMULATIONS OF THE NEP APPROACH

The first NEP, called NEP1, was proposed in Ref. 41. An improved version, called NEP2, was presented in Ref. 42. In the present paper, we further refine the NEP approach and introduce NEP3. In this section, we present NEP3 and discuss the differences to NEP1 and NEP2.

A. The neural-network model

Following Behler and Parrinello,⁴⁹ the site energy of atom i is taken as a function of the descriptor vector with N_{des} components, $U_i(\mathbf{q}) = U_i\left(\{q_\nu^i\}_{\nu=1}^{N_{\text{des}}}\right)$. We use a feedforward neural-network with a single hidden layer with N_{neu} neurons to model this function:

$$U_i = \sum_{\mu=1}^{N_{\text{neu}}} w_\mu^{(1)} \tanh \left(\sum_{\nu=1}^{N_{\text{des}}} w_{\mu\nu}^{(0)} q_\nu^i - b_\mu^{(0)} \right) - b^{(1)}, \quad (1)$$

where $\tanh(x)$ is the activation function in the hidden layer, $\mathbf{w}^{(0)}$ is the connection weight matrix from the input layer (descriptor vector) to the hidden layer, $\mathbf{w}^{(1)}$ is the connection weight vector from the hidden layer to the output node, which is the energy U_i , $\mathbf{b}^{(0)}$ is the bias vector in the hidden layer, and $b^{(1)}$ is the bias for node U_i . The total number of parameters in the neural network is thus $(N_{\text{des}} + 2)N_{\text{neu}} + 1$. The descriptor vector is formed by juxtaposition of a number of components, including those with radial (distance) information only, which are called radial descriptor components, and those with both radial and angular information, which are called angular descriptor components. The descriptor is one of the most important aspects in MLPs.^{50,51} We discuss the radial and angular descriptor components below.

B. Radial descriptor components

There are $n_{\max}^R + 1$ radial descriptor components and they are defined as

$$q_n^i = \sum_{j \neq i} g_n(r_{ij}) \quad \text{with} \quad 0 \leq n \leq n_{\max}^R, \quad (2)$$

where the summation runs over all the neighbors of atom i within a certain cutoff distance. The functions $g_n(r_{ij})$ depend on the distance r_{ij} only and are therefore called the radial functions. In NEP3, they are defined as a linear combination of $N_{\text{bas}}^R + 1$ basis functions $\{f_k(r_{ij})\}_{k=0}^{N_{\text{bas}}^R}$:

$$g_n(r_{ij}) = \sum_{k=0}^{N_{\text{bas}}^R} c_{nk}^{ij} f_k(r_{ij}) \quad \text{with} \quad (3)$$

$$f_k(r_{ij}) = \frac{1}{2} \left[T_k \left(2 \left(r_{ij}/r_c^R - 1 \right)^2 - 1 \right) + 1 \right] f_c(r_{ij}). \quad (4)$$

Both n_{\max}^R and N_{bas}^R are tunable hyperparameters in NEP3 which, along with other ones, will be listed in Sect. IIH2. In Sect. IIIB, we will use a few examples to illustrate the judicious choice of the various hyperparameters in typical applications. Here, $T_k(x)$ is the k -th order Chebyshev polynomial of the first kind and $f_c(r_{ij})$ is the cutoff function defined as

$$f_c(r_{ij}) = \begin{cases} \frac{1}{2} \left[1 + \cos \left(\pi \frac{r_{ij}}{r_c^R} \right) \right] & r_{ij} \leq r_c^R \\ 0 & r_{ij} > r_c^R \end{cases} \quad (5)$$

Here, r_c^R is the cutoff distance of the radial descriptor components. The expansion coefficients c_{nk}^{ij} depend on n and k and also on the types of atoms i and j . Due to the summation over neighbors, the radial descriptor components defined above are invariant with respect to permutation of atoms of the same type.

If the material considered has N_{typ} atom types, the number of c_{nk}^{ij} coefficients for the radial descriptor components is $N_{\text{typ}}^2 (n_{\max}^R + 1) (N_{\text{bas}}^R + 1)$. In NEP2, each radial function is simply a basis function and c_{nk}^{ij} is reduced to $\delta_{nk} c_{nij}$, where δ_{nk} is the Kronecker symbol and c_{nij} is defined in Ref. 42. In NEP2 and NEP3, these coefficients are trainable (similar to the parameters in the neural network), while in NEP1, we have used some fixed coefficients similar to previous works.^{14,52} In Ref. 42, we have shown that NEP2 is much more accurate than NEP1 for multi-component systems. In this paper, we will show that the accuracy of NEP3 for multi-component systems is further improved compared to NEP2.

C. Angular descriptor components

In NEP1 and NEP2 the angular descriptor components $\{q_{nl}^i\}$ are taken as ($1 \leq l \leq l_{\max}^{3b}$):

$$q_{nl}^i = \frac{2l+1}{4\pi} \sum_{j \neq i} \sum_{k \neq i} g_n(r_{ij}) g_n(r_{ik}) P_l(\cos \theta_{ijk}), \quad (6)$$

where $P_l(\cos \theta_{ijk})$ is the Legendre polynomial of order l and θ_{ijk} is the angle formed by the ij and ik bonds. The radial functions $g_n(r_{ij})$ have the same forms as in Eq. (3), but can have a different cutoff distance r_c^A and a different basis size N_{bas}^A than those in the radial descriptor components. Usually, it is beneficial to use $r_c^A < r_c^R$, assuming that there is no directional dependence of the descriptor on some neighboring atoms that are sufficiently far away from the central atom. This reflects the physical intuition that interaction strength decreases both with distance and order. The radial descriptor components are relatively cheap to evaluate and one can thus use a relatively large radial cutoff distance r_c^R (also relatively large n_{\max}^R and N_{bas}^R) combined with a relatively small angular cutoff distance r_c^A (also relatively small n_{\max}^A and N_{bas}^A) to achieve a good balance between accuracy and speed. Note that message-passing could effectively increase the interaction range but is not necessarily an efficient way of describing long-range interactions.⁵³ Using a relatively large cutoff for the radial descriptor components is generally a more efficient way of incorporating long-ranged interactions, such as van-der-Waals (vdW) and screened Coulomb interactions, although it is incapable of describing genuine long-ranged interactions such as unscreened Coulomb interactions.

The expression (6) is not efficient for numerical evaluation due to the double summation over neighbors. An equivalent form that is more efficient for numerical evaluation can be obtained by using the addition theorem of the spherical harmonics as:

$$q_{nl}^i = \sum_{m=-l}^l (-1)^m A_{nlm}^i A_{nl(-m)}^i = \sum_{m=0}^l (2 - \delta_{0l}) |A_{nlm}^i|^2, \quad (7)$$

where

$$A_{nlm}^i = \sum_{j \neq i} g_n(r_{ij}) Y_{lm}(\theta_{ij}, \phi_{ij}). \quad (8)$$

Here, $Y_{lm}(\theta_{ij}, \phi_{ij})$ are the spherical harmonics as a function of the polar angle θ_{ij} and the azimuthal angle ϕ_{ij} for the position difference vector $\mathbf{r}_{ij} \equiv \mathbf{r}_j - \mathbf{r}_i$ from atom i to atom j . In Eq. (7), we have used the property $A_{nl(-m)} = (-1)^m A_{nlm}^*$, which follows from the property $Y_{l(-m)} = (-1)^m Y_{lm}^*$.

The angular descriptor components above are usually known as 3-body ones as in the ACE approach,⁴⁶ although all the descriptor components are many-body in nature. For simplicity, we will use the ACE terminology. Higher-order angular descriptor components can be similarly constructed.⁴⁶ In NEP3, we add the following 4-body descriptor components ($1 \leq l_1 \leq l_2 \leq l_3 \leq l_{\max}^{4b}$):

$$q_{nl_1 l_2 l_3}^i = \sum_{m_1=-l_1}^{l_1} \sum_{m_2=-l_2}^{l_2} \sum_{m_3=-l_3}^{l_3} \begin{pmatrix} l_1 & l_2 & l_3 \\ m_1 & m_2 & m_3 \end{pmatrix} \times A_{nl_1 m_1}^i A_{nl_2 m_2}^i A_{nl_3 m_3}^i, \quad (9)$$

and the following 5-body ones ($1 \leq l_1 \leq l_2 \leq l_3 \leq l_4 \leq l_{\max}^{5b}$):

$$q_{nl_1l_2l_3l_4}^i = \sum_{m_1=-l_1}^{l_1} \sum_{m_2=-l_2}^{l_2} \sum_{m_3=-l_3}^{l_3} \sum_{m_4=-l_4}^{l_4} \begin{bmatrix} l_1 & l_2 & l_3 & l_4 \\ m_1 & m_2 & m_3 & m_4 \end{bmatrix} A_{nl_1m_1}^i A_{nl_2m_2}^i A_{nl_3m_3}^i A_{nl_4m_4}^i, \quad (10)$$

where $\begin{bmatrix} l_1 & l_2 & l_3 \\ m_1 & m_2 & m_3 \end{bmatrix}$ are Wigner $3j$ symbols and⁴⁶

$$\begin{bmatrix} l_1 & l_2 & l_3 & l_4 \\ m_1 & m_2 & m_3 & m_4 \end{bmatrix} = \sum_{L=\max\{|l_1-l_2|, |l_3-l_4|\}}^{\min\{|l_1+l_2|, |l_3+l_4|\}} \sum_{M=-L}^L (-1)^M \begin{pmatrix} L & l_1 & l_2 \\ -M & m_1 & m_2 \end{pmatrix} \begin{pmatrix} L & l_3 & l_4 \\ M & m_3 & m_4 \end{pmatrix}. \quad (11)$$

We can consider higher-order terms,⁴⁶ but to keep a balance between accuracy and speed, we only consider those up to fifth order. Recent work suggests that 4-body interactions are difficult to learn using only 3-body correlations⁵⁴ and that using only up to 4-body correlations can still yield identical results for different configurations of simple molecules.⁵⁵ One can formally achieve completeness in the MTP formalism,³⁰ the ACE formalism,^{46,48} and other related ones,⁵⁶⁻⁵⁸ but in practice, there is always a truncation of the descriptor size and a balance must be struck between accuracy and speed. This balance is one of the most important guidelines for the development of NEP in GPUMD.

D. Explicit expressions of the angular descriptor components

The angular descriptor components are quite complicated and care must be taken to achieve an efficient implementation. There have been some implementations of the ACE approach combined with linear regression, where it has been found that recursive evaluation can lead to much higher efficiency.^{35,36,48} In our GPU implementation of NEP3 with the ACE-like descriptor components, we find it crucial to derive the relevant expressions as explicitly as possible as it allows us to reduce the number of terms to be evaluated thanks to symmetry considerations.

To facilitate the following presentation, we define a series of summations that are used to express the angular descriptor components ($0 \leq n \leq n_{\max}^A$ and $0 \leq k \leq 23$):

$$S_{n,k} = \sum_{j \neq i} \frac{g_n(r_{ij})}{r_{ij}^n} b_k(x_{ij}, y_{ij}, z_{ij}). \quad (12)$$

The functions $b_k(x_{ij}, y_{ij}, z_{ij})$ here are z_{ij} , x_{ij} , y_{ij} , $3z_{ij}^2 - r_{ij}^2$, $x_{ij}z_{ij}$, $y_{ij}z_{ij}$, $x_{ij}^2 - y_{ij}^2$, $2x_{ij}y_{ij}$, $(5z_{ij}^2 - 3r_{ij}^2)z_{ij}$, $(5z_{ij}^2 - r_{ij}^2)x_{ij}$, $(5z_{ij}^2 - r_{ij}^2)y_{ij}$, $(x_{ij}^2 - y_{ij}^2)z_{ij}$, $2x_{ij}y_{ij}z_{ij}$, $(x_{ij}^2 -$

$3y_{ij}^2)x_{ij}$, $(3x_{ij}^2 - y_{ij}^2)y_{ij}$, $(35z_{ij}^2 - 30r_{ij}^2)z_{ij}^2 + 3r_{ij}^4$, $(7z_{ij}^2 - 3r_{ij}^2)x_{ij}z_{ij}$, $(7z_{ij}^2 - 3r_{ij}^2)y_{ij}z_{ij}$, $(7z_{ij}^2 - r_{ij}^2)(x_{ij}^2 - y_{ij}^2)$, $(7z_{ij}^2 - r_{ij}^2)2x_{ij}y_{ij}$, $(x_{ij}^2 - 3y_{ij}^2)x_{ij}z_{ij}$, $(3x_{ij}^2 - y_{ij}^2)y_{ij}z_{ij}$, $(x_{ij}^2 - y_{ij}^2)^2 - 4x_{ij}^2y_{ij}^2$, and $4(x_{ij}^2 - y_{ij}^2)x_{ij}y_{ij}$ from $k = 0$ to $k = 23$. With these summations, we can write the 3-body angular descriptor components up to $l_{\max}^{3b} = 4$ explicitly as:

$$q_{n1}^i = \frac{1}{4} \frac{3}{\pi} S_{n,0}^2 + 2 \frac{1}{4} \frac{3}{2\pi} (S_{n,1}^2 + S_{n,2}^2) \equiv \sum_{k=0}^2 C_k^{3b} S_{n,k}^2; \quad (13)$$

$$q_{n2}^i = \frac{1}{16} \frac{5}{\pi} S_{n,3}^2 + 2 \frac{1}{4} \frac{15}{2\pi} (S_{n,4}^2 + S_{n,5}^2) + 2 \frac{1}{16} \frac{15}{2\pi} (S_{n,6}^2 + S_{n,7}^2) \equiv \sum_{k=3}^7 C_k^{3b} S_{n,k}^2; \quad (14)$$

$$q_{n3}^i = \frac{1}{16} \frac{7}{\pi} S_{n,8}^2 + 2 \frac{1}{64} \frac{21}{\pi} (S_{n,9}^2 + S_{n,10}^2) + 2 \frac{1}{16} \frac{105}{2\pi} (S_{n,11}^2 + S_{n,12}^2) + 2 \frac{1}{64} \frac{35}{\pi} (S_{n,13}^2 + S_{n,14}^2) \equiv \sum_{k=8}^{14} C_k^{3b} S_{n,k}^2; \quad (15)$$

$$q_{n4}^i = \frac{9}{256} \frac{1}{\pi} S_{n,15}^2 + 2 \frac{9}{64} \frac{5}{\pi} (S_{n,16}^2 + S_{n,17}^2) + 2 \frac{9}{64} \frac{5}{2\pi} (S_{n,18}^2 + S_{n,19}^2) + 2 \frac{9}{64} \frac{35}{\pi} (S_{n,20}^2 + S_{n,21}^2) + 2 \frac{9}{256} \frac{35}{2\pi} (S_{n,22}^2 + S_{n,23}^2) \equiv \sum_{k=15}^{23} C_k^{3b} S_{n,k}^2, \quad (16)$$

whereby we defined the 3-body coefficients $\{C_k^{3b}\}_{k=0}^{23}$.

For 4-body angular descriptor components, we only consider the case of $l_1 = l_2 = l_3$ and up to $l_{\max}^{4b} = 2$. It turns out that $q_{n111}^i = q_{n333}^i = 0$. Therefore, there is no difference between $l_{\max}^{4b} = 2$ and $l_{\max}^{4b} = 3$. Then we only have the case of $l_1 = l_2 = l_3 = 2$,

$$q_{n222}^i = -\sqrt{\frac{2}{35}} A_{n20}^i A_{n20}^i A_{n20}^i + 6\sqrt{\frac{1}{70}} A_{n20}^i A_{n21}^i A_{n2(-1)}^i + 6\sqrt{\frac{2}{35}} A_{n20}^i A_{n22}^i A_{n2(-2)}^i - 6\sqrt{\frac{3}{35}} A_{n21}^i A_{n21}^i A_{n2(-2)}^i. \quad (17)$$

The root-rational-fraction package⁵⁹ has been used to obtain analytical expressions of the various Wigner $3j$ sym-

bols. With some algebra, we have

$$\begin{aligned}
q_{n222}^i &= -\sqrt{\frac{2}{35}} \left(\frac{1}{4} \sqrt{\frac{5}{\pi}} \right)^3 S_{n,3}^3 \\
&\quad - 6\sqrt{\frac{1}{70}} \left(\frac{1}{4} \sqrt{\frac{5}{\pi}} \right) \left(\frac{1}{2} \sqrt{\frac{15}{2\pi}} \right)^2 S_{n,3}(S_{n,4}^2 + S_{n,5}^2) \\
&\quad + 6\sqrt{\frac{2}{35}} \left(\frac{1}{4} \sqrt{\frac{5}{\pi}} \right) \left(\frac{1}{4} \sqrt{\frac{15}{2\pi}} \right)^2 S_{n,3}(S_{n,6}^2 + S_{n,7}^2) \\
&\quad + 6\sqrt{\frac{3}{35}} \left(\frac{1}{2} \sqrt{\frac{15}{2\pi}} \right)^2 \left(\frac{1}{4} \sqrt{\frac{15}{2\pi}} \right) S_{n,6}(S_{n,5}^2 - S_{n,4}^2) \\
&\quad - 12\sqrt{\frac{3}{35}} \left(\frac{1}{2} \sqrt{\frac{15}{2\pi}} \right)^2 \left(\frac{1}{4} \sqrt{\frac{15}{2\pi}} \right) S_{n,4}S_{n,5}S_{n,7} \\
&\equiv C_0^{4b} S_{n,3}^3 + C_1^{4b} S_{n,3}(S_{n,4}^2 + S_{n,5}^2) \\
&\quad + C_2^{4b} S_{n,3}(S_{n,6}^2 + S_{n,7}^2) \\
&\quad + C_3^{4b} S_{n,6}(S_{n,5}^2 - S_{n,4}^2) + C_4^{4b} S_{n,4}S_{n,5}S_{n,7}, \quad (18)
\end{aligned}$$

whereby we defined the 4-body coefficients $\{C_k^{4b}\}_{k=0}^4$.

For 5-body descriptors, we only consider up to $l_1 = l_2 = l_3 = l_4 = 1$,

$$\begin{aligned}
q_{n1111}^i &= \frac{7}{15} (A_{n10}^i)^4 - \frac{28}{15} (A_{n10}^i)^2 A_{n11}^i A_{n1(-1)}^i \\
&\quad + \frac{28}{15} (A_{n11}^i)^2 (A_{n1(-1)}^i)^2 \\
&= \frac{7}{20\pi} S_{n,0}^4 + \frac{7}{10\pi} S_{n,0}^2 (S_{n,1}^2 + S_{n,2}^2) \\
&\quad + \frac{7}{10\pi} (S_{n,1}^2 + S_{n,2}^2)^2 \\
&\equiv C_0^{5b} S_{n,0}^4 + C_1^{5b} S_{n,0}^2 (S_{n,1}^2 + S_{n,2}^2) \\
&\quad + C_2^{5b} (S_{n,1}^2 + S_{n,2}^2)^2, \quad (19)
\end{aligned}$$

whereby we defined the 5-body coefficients $\{C_k^{5b}\}_{k=0}^2$.

In our implementation, the 3-body coefficients $\{C_k^{3b}\}_{k=0}^{23}$, 4-body coefficients $\{C_k^{4b}\}_{k=0}^4$, and 5-body coefficients $\{C_k^{5b}\}_{k=0}^2$ are pre-computed. This is crucial for obtaining high computational performance.

We can now enumerate the descriptor vector length. There are $(n_{\max}^R + 1)$ radial descriptor components, $(n_{\max}^A + 1)l_{\max}^{3b}$ 3-body descriptor components, $(n_{\max}^A + 1)$ 4-body descriptor components, and $(n_{\max}^A + 1)$ 5-body descriptor components. Therefore, we have

$$N_{\text{des}} = (n_{\max}^R + 1) + (n_{\max}^A + 1) (l_{\max}^{3b} + 2) \quad (20)$$

in NEP3 if we include both the 4-body and the 5-body descriptor components.

E. Force, virial, and heat current expressions

As stressed in Ref. 44, we need to derive an explicit expression of the partial force⁶⁰ for an efficient GPU implementation.

The partial force is

$$\begin{aligned}
\frac{\partial U_i}{\partial \mathbf{r}_{ij}} &= \sum_{n=0}^{n_{\max}^R} \frac{\partial U_i}{\partial q_n^i} \frac{\partial q_n^i}{\partial \mathbf{r}_{ij}} + \sum_{n=0}^{n_{\max}^A} \sum_{l=1}^{l_{\max}^{3b}} \frac{\partial U_i}{\partial q_{nl}^i} \frac{\partial q_{nl}^i}{\partial \mathbf{r}_{ij}} \\
&\quad + \sum_{n=0}^{n_{\max}^A} \sum_{l=1}^{l_{\max}^{4b}} \frac{\partial U_i}{\partial q_{nlll}^i} \frac{\partial q_{nlll}^i}{\partial \mathbf{r}_{ij}} + \sum_{n=0}^{n_{\max}^A} \sum_{l=1}^{l_{\max}^{5b}} \frac{\partial U_i}{\partial q_{nllll}^i} \frac{\partial q_{nllll}^i}{\partial \mathbf{r}_{ij}}. \quad (21)
\end{aligned}$$

Because all the relevant functions here are analytical, it is straightforward to derive explicit expressions for all the partial derivatives in the equation above.

With the partial force available, the total force acting on atom i from atom j can be computed as⁶⁰

$$\mathbf{F}_{ij} = \frac{\partial U_i}{\partial \mathbf{r}_{ij}} - \frac{\partial U_j}{\partial \mathbf{r}_{ji}}, \quad (22)$$

which respects Newton's third law $\mathbf{F}_{ij} = -\mathbf{F}_{ji}$. The total force acting on atom i from all the neighboring atoms is thus

$$\mathbf{F}_i = \sum_{j \neq i} \mathbf{F}_{ij}. \quad (23)$$

From the partial force, one can define the per-atom virial^{60,61}

$$\mathbf{W}_i = \sum_{j \neq i} \mathbf{r}_{ij} \otimes \frac{\partial U_j}{\partial \mathbf{r}_{ji}}. \quad (24)$$

By contracting the per-atom virial above with the velocity \mathbf{v}_i , one can then obtain the per-atom heat current:^{60,61}

$$\begin{aligned}
\mathbf{J}_i &= \mathbf{W}_i \cdot \mathbf{v}_i = \sum_{j \neq i} \left(\mathbf{r}_{ij} \otimes \frac{\partial U_j}{\partial \mathbf{r}_{ji}} \right) \cdot \mathbf{v}_i \\
&= \sum_{j \neq i} \mathbf{r}_{ij} \left(\frac{\partial U_j}{\partial \mathbf{r}_{ji}} \cdot \mathbf{v}_i \right). \quad (25)
\end{aligned}$$

The total heat current in the system is the sum of the per-atom contributions:

$$\mathbf{J} = \sum_i \mathbf{J}_i = \sum_i \sum_{j \neq i} \mathbf{r}_{ij} \left(\frac{\partial U_j}{\partial \mathbf{r}_{ji}} \cdot \mathbf{v}_i \right). \quad (26)$$

By an exchange of dummy indices, we can also write Eq. (26) as

$$\mathbf{J} = - \sum_i \sum_{j \neq i} \mathbf{r}_{ij} \left(\frac{\partial U_i}{\partial \mathbf{r}_{ij}} \cdot \mathbf{v}_j \right). \quad (27)$$

Both Eqs. (26) and (27) can be used in the Green-Kubo method for thermal conductivity calculations, but Eq. (26) is a more convenient form for the homogeneous non-equilibrium molecular dynamics (HNEMD) method and the related spectral decomposition method, as it does

not involved the velocities \mathbf{v}_j of the neighboring atoms j for a given atom i .

The heat current expressions above apply to all the interatomic potentials implemented in GPUMD. In all the cases, the validity of the heat current expressions has been numerically confirmed in terms of energy conservation.^{62–65} Equation (27) has been recently used in an on-the-fly MLP.⁶⁶ Since the only assumptions for the derivations⁶⁰ of these expressions are the locality properties of the interatomic potentials, our heat current expressions generally apply to the multi-body cluster potentials as considered in Ref. 67, as we show in Appendix A.

F. Loss function and training algorithm

We use the separable natural evolution strategy (SNES)⁶⁸ to optimize the free parameters in NEP. We denote a set of parameters as a vector \mathbf{z} , whose dimension is the total number of parameters N_{par} . In NEP1,

$$N_{\text{par}} = (N_{\text{des}} + 2)N_{\text{neu}} + 1, \quad (28)$$

which is the same for both single-component and multi-component systems. In NEP2, we added trainable parameters to the descriptor for multi-component systems and we have

$$N_{\text{par}} = (N_{\text{des}} + 2)N_{\text{neu}} + 1 + N_{\text{typ}}^2(n_{\text{max}}^{\text{R}} + n_{\text{max}}^{\text{A}} + 2), \quad (29)$$

if $N_{\text{typ}} > 1$, and the same N_{par} as in NEP1 if $N_{\text{typ}} = 1$. In NEP3, the number of trainable parameters in the descriptor is increased for both single and multi-component systems and we have

$$\begin{aligned} N_{\text{par}} = & (N_{\text{des}} + 2)N_{\text{neu}} + 1 \\ & + N_{\text{typ}}^2(n_{\text{max}}^{\text{R}} + 1)(N_{\text{bas}}^{\text{R}} + 1) \\ & + N_{\text{typ}}^2(n_{\text{max}}^{\text{A}} + 1)(N_{\text{bas}}^{\text{A}} + 1). \end{aligned} \quad (30)$$

We can formally express the loss function as a function of the free parameters,

$$L = L(\mathbf{z}), \quad (31)$$

and express the training process as a real-valued optimization problem:

$$\mathbf{z}^* = \arg \min_{\mathbf{z}} L(\mathbf{z}), \quad (32)$$

where \mathbf{z}^* is an optimal set of parameters.

The total loss function is defined as a weighted sum of

all these individual loss functions:

$$\begin{aligned} L(\mathbf{z}) = & \lambda_e \left(\frac{1}{N_{\text{str}}} \sum_{n=1}^{N_{\text{str}}} (U^{\text{NEP}}(n, \mathbf{z}) - U^{\text{tar}}(n))^2 \right)^{1/2} \\ & + \lambda_f \left(\frac{1}{3N} \sum_{i=1}^N (\mathbf{F}_i^{\text{NEP}}(\mathbf{z}) - \mathbf{F}_i^{\text{tar}})^2 \right)^{1/2} \\ & + \lambda_v \left(\frac{1}{6N_{\text{str}}} \sum_{n=1}^{N_{\text{str}}} \sum_{\mu\nu} (W_{\mu\nu}^{\text{NEP}}(n, \mathbf{z}) - W_{\mu\nu}^{\text{tar}}(n))^2 \right)^{1/2} \\ & + \lambda_1 \frac{1}{N_{\text{par}}} \sum_{n=1}^{N_{\text{par}}} |z_n| \\ & + \lambda_2 \left(\frac{1}{N_{\text{par}}} \sum_{n=1}^{N_{\text{par}}} z_n^2 \right)^{1/2}, \end{aligned} \quad (33)$$

where N_{str} is the number of structures in the training data set (if using a full batch) or the number of structures in a mini-batch and N is the total number of atoms in these structures. $U^{\text{NEP}}(n, \mathbf{z})$ and $W_{\mu\nu}^{\text{NEP}}(n, \mathbf{z})$ are per-atom energy and virial tensor predicted by the NEP with parameters \mathbf{z} for the n -th structure, and $\mathbf{F}_i^{\text{NEP}}(\mathbf{z})$ is the predicted force for the i th atom. $U^{\text{tar}}(n)$, $W_{\mu\nu}^{\text{tar}}(n)$ and $\mathbf{F}_i^{\text{tar}}$ are the corresponding target values. That is, the loss functions for energy, force, and virial are defined as their root mean square errors (RMSEs) between the current NEP predictions and the target values. The last two terms represent ℓ_1 and ℓ_2 regularization. The weights λ_e , λ_f , λ_v , λ_1 , and λ_2 are tunable hyper-parameters. When calculating the loss function, we use the following units: eV/atom for energy and virial and eV/Å for force components.

The SNES⁶⁸ we use for optimizing Eq. (33) is a principled approach to real-valued evolutionary optimization by following the natural gradient of the loss function to update a search distribution (a mean value and a variance for each trainable parameter) for a population of solutions. It is a derivative-free black-box optimizer and thus does not require the loss function to have any analytical properties. An explicit workflow of the training algorithm has been presented in Ref. 41.

G. GPU implementation

The NEP approach is implemented in the open-source GPUMD package, which is a general-purpose molecular dynamics (MD) simulation package fully implemented on GPUs. It currently supports only Nvidia GPUs and the programming language is CUDA C++. In this section as well as Appendix B, we present the detailed algorithms for our CUDA implementation of the NEP approach.

Similar to many other MLPs, NEP is a many-body potential and is very similar to empirical many-body potentials such as the EAM potential⁴⁰ and the Tersoff

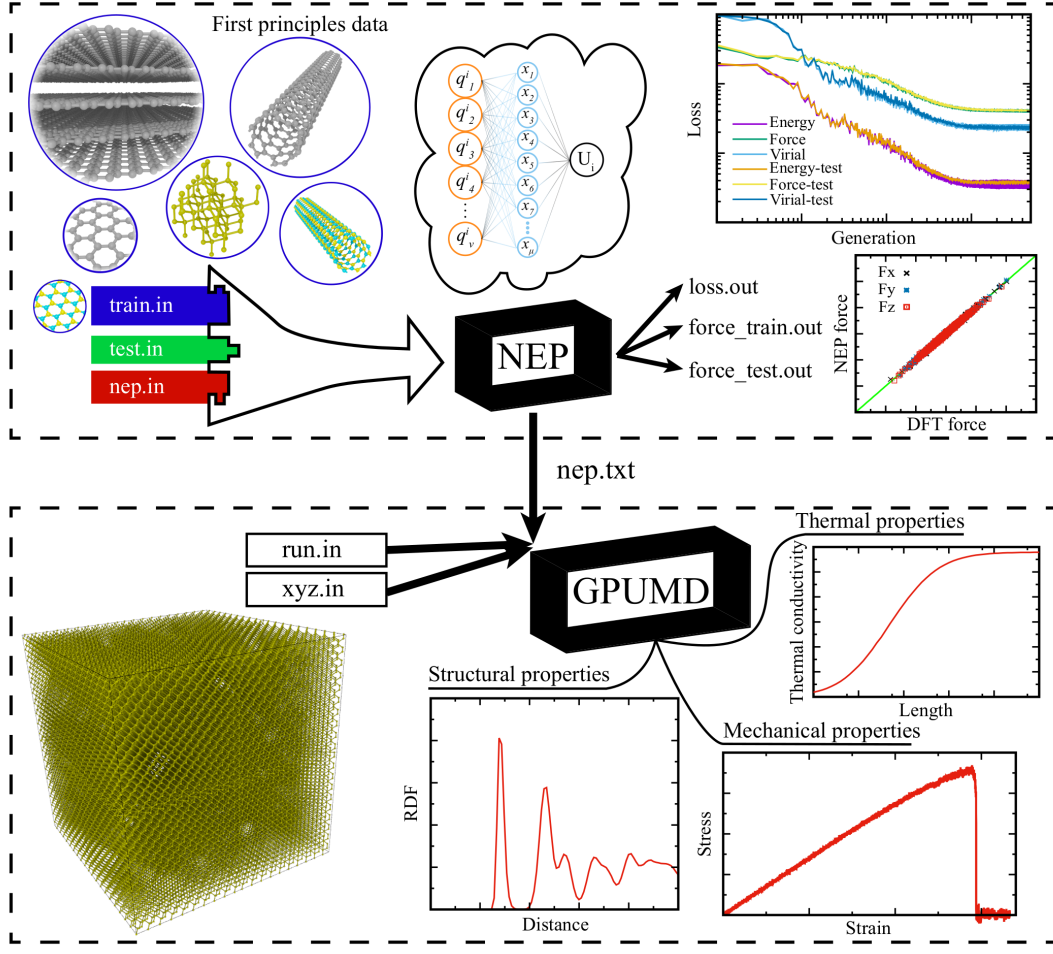


FIG. 1. The GPUMD package includes two executables, `gpumd` and `nep`, which are represented by the two black boxes. The `nep` program can be used for training NEP models and the `gpumd` program can be used to perform atomistic simulations using the trained potentials. See text for details.

potential.³⁸ Specifically, the radial descriptor part resembles an EAM potential and the angular descriptor part resembles a Tersoff potential. Therefore, our CUDA implementation of the NEP approach follows the established efficient scheme for empirical many-body potentials.⁴⁴

The overall strategy of our CUDA implementation of the NEP approach is to use a few CUDA kernels only, which ensures a high degree of parallelism and high arithmetic intensity, both of which are crucial for achieving high performance in CUDA programming. In all the CUDA kernels, one CUDA thread is assigned to one atom, i.e., there is a one-to-one correspondence between atoms and CUDA threads. The descriptor vector and the various per-atom quantities, including the site energy, force, and virial for one atom, are all calculated within one CUDA thread. This also includes the application of the neural network as represented by Eq. (1). Appendix B1 shows the CUDA `__device__` function (to be called in the first CUDA kernel function as discussed below) evaluating Eq. (1) as well as $\{\partial U_i / \partial q_\nu^i\}$. One

can see that the feedforward neural network used here is an analytical multi-variable scalar function.

The evaluation of NEP related quantities (energy, force, and virial) requires 4 CUDA kernels only:

1. The first CUDA kernel calculates the whole descriptor vector and applies the neural network to obtain the site energy and the derivatives of the energy with respect to the descriptor components, see Algorithm 1 in Appendix B.
2. The second CUDA kernel calculates the force and virial related to the radial descriptor components, see Algorithm 2 in Appendix B.
3. The third CUDA kernel calculates the partial force related to the angular descriptor components, see Algorithm 3 in Appendix B.
4. The fourth CUDA kernel calculates the force and virial related to the angular descriptor components, see Algorithm 4 in Appendix B.

In these CUDA kernels, the inputs and outputs related to the atoms (position, energy, force, and virial) are all in double precision, but the internal calculations within the CUDA kernels are mostly in single precision. This is an effective mixed-precision approach which can keep a good balance between accuracy and efficiency that has been adopted in many other GPU-accelerated atomistic simulation packages.^{69–71}

H. Training and using NEPs

1. Overview of the GPUMD package

The GPUMD package^{43,44} can be used to train NEPs and use them in atomistic simulations. GPUMD can be compiled and used in both Linux and Windows, provided that a CUDA development environment and a CUDA-enabled GPU are available. After compilation, one obtains the `nep` and `gpumd` executable, which can be used to train and use NEPs, respectively. Figure 1 provides a schematic overview of the workflow of training and using NEPs.

The GPUMD package started from a minimal CUDA code implementing only simple pairwise potentials and thermal conductivity calculations.⁴³ Gradually, empirical many-body potentials were implemented using the unique formalism we proposed,^{44,60} including the Tersoff³⁸ and Tersoff-like⁷² potentials, the Stillinger-Weber potential,⁷³ and EAM potentials.⁴⁰ Recently, support was also added for machine-learned force constant potentials constructed using the HIPHIVE package^{74–65}. The most recent addition are the various versions of NEP as developed in the previous papers^{41,42} as well as the current one.

Apart from supporting the above important interatomic potentials, GPUMD also supports many statistical ensembles, including the NVE (microcanonical), NVT (isothermal), and NPT (isothermal-isobaric) ensembles. For the NVT ensemble, it has options for the Berendsen thermostat,⁷⁵ the Nosé-Hoover chain thermostat,^{76–78} the Bussi-Donadio-Parrinello thermostat,⁷⁹ and the Langevin thermostat in different flavors.^{80,81} For the NPT ensemble, GPUMD supports the classical Berendsen barostat⁷⁵ and the recently proposed stochastic cell-rescaling barostat by Bernetti and Bussi.⁸²

GPUMD has been mainly used to study thermal transport. It supports the equilibrium MD method based on the Green-Kubo relation,^{83,84} the non-equilibrium MD method using two or more thermostats (preferably the Langevin thermostats⁸⁵), and the HNEMD method using a homogeneous driving force.^{86,87} The thermal transport coefficients, either thermal conductance or thermal conductivity, can be decomposed both spatially and spectrally.^{61,63,87} GPUMD has been used to establish the best practices^{85,88} in MD simulations of thermal transport. It has also been used to study the particular thermal transport properties of specific materials, in-

cluding various two-dimensional (2D) materials,^{64,89–103} vdW structures based on 2D materials,^{104–110} and quasi-one-dimensional materials.^{111–113} There are applications focused on revealing unique phonon transport mechanisms.^{114–120} The high efficiency of GPUMD also enabled high-throughput thermal transport simulations that were used as training/testing data for machine learning models of interfacial thermal transport.¹²¹

Although previous studies using GPUMD have been mostly focused on thermal transport properties, GPUMD has already been developed into a general-purpose atomistic simulation package. In Sect. V we will showcase a series of typical atomistic simulations using a NEP model for carbon systems trained in this paper.

2. Training a NEP model

To train a NEP model, one needs to prepare three input files: `train.in`, `test.in`, and `nep.in`. The first two contain the training and the testing data, respectively. The files `train.in` and `test.in` have the same data format, the only difference being that the data in `train.in` will be used for training and those in `test.in` will be used for testing. The file `train.in` (`test.in`) contains the following data: the number of structures in the training (testing) set, the reference energy, reference virial tensor (optional), and cell metric for each structure, as well as the chemical symbol, position vector, and reference force vector for each atom in each structure. For the specific data format, we refer the reader to the GPUMD manual.

The file `nep.in` contains hyper-parameters that define the NEP model and control the training process. In this file, one can choose the NEP version (currently NEP2 or NEP3), specify the number of atom types and their chemical symbols, the cutoff distances r_c^R and r_c^A , the radial function parameters (n_{\max}^R , n_{\max}^A , N_{bas}^R , and N_{bas}^A), the angular expansion parameters (l_{\max}^{3b} , l_{\max}^{4b} , and l_{\max}^{5b}), the weights for the different terms in the loss function (λ_e , λ_f , λ_v , λ_1 , and λ_2), the number of neurons N_{neu} in the hidden layer of the neural network, the batch size N_{bat} (number of structures in one batch), the population size N_{pop} , and the number of generations N_{gen} in the SNES training algorithm. Details concerning the `nep.in` file are presented in the GPUMD manual.

During the training process, predicted energy, force, virial values, the various terms of the loss function (both for the training and the testing data sets), the potential file, and a file used for restarting are continuously updated. Further details concerning the output files of the `nep` executable can be found in the GPUMD manual.

3. Using a NEP

The potential file `nep.txt` contains all the information that constitutes a NEP model and can be used directly as an input to the `gpumd` executable for running atomistic

simulations. To use the `gpumd` executable, one needs to prepare another input file, `run.in`, which specifies the simulation process. Several examples are presented in Sect. V below.

III. PERFORMANCE OF NEP MODELS

A. NEP3 vs NEP2

In this section, we demonstrate the workflow of using the `nep` executable to train NEPs and show the enhanced accuracy of NEP3 compared to NEP2 due to the improved radial functions. Here we use the MgAlCu alloy system, which has been studied previously using a DP.¹²² There are 141,409 structures and we used 90% of this set for training and 10% for testing. There are tools in the GPUMD package for preparing the required `train.in` and `test.in` input files for the `nep` executable.

TABLE I. RMSEs for energies, forces, and virials for the MgAlCu alloy system using NEP2 and NEP3.

RMSE	NEP2	NEP3
Energies (meV/atom)	11	10
Forces (meV/Å)	68	63
Virials (meV/atom)	43	41

The other input file needed for the `nep` executable is `nep.in`. For our test using NEP2, this file reads as follows:

```
version      2
type        3 Cu Al Mg
cutoff      6 3.5
n_max      15 10
l_max       4
neuron      50
lambda_1    0.05
lambda_2    0.05
lambda_e    1.0
lambda_f    1.0
lambda_v    0.1
batch       1000
population  50
generation  500000
```

For our test using NEP3, it reads:

```
version      3
type        3 Cu Al Mg
cutoff      6 3.5
n_max      12 8
basis_size  12 8
l_max       4
neuron      50
lambda_1    0.05
lambda_2    0.05
```

lambda_e	1.0
lambda_f	1.0
lambda_v	0.1
batch	1000
population	50
generation	500000

The only differences between the hyperparameters used for NEP2 and NEP3 are related to the radial functions. For NEP2, we use $n_{\max}^R = 15$ and $n_{\max}^A = 10$. For NEP3, we use $n_{\max}^R = N_{\text{bas}}^R = 12$ and $n_{\max}^A = N_{\text{bas}}^A = 8$. The reason for using smaller n_{\max}^R and n_{\max}^A values in NEP3 compared to NEP2 is that one radial function in NEP3 is a linear combination of a few basis functions, while one radial function in NEP2 is simply one basis function. Even in this case, NEP3 can achieve a noticeably higher accuracy compared to NEP2, as shown in Table I. With these parameters, NEP3 still has a similar computational speed as NEP2 in MD simulations, reaching about 1.5×10^7 atom step/s using one Tesla A100 GPU.

The `nep` executable produces a number of output files that can be used to examine the training/testing results in detail. Figure 2 shows the training and testing RMSEs as well as the loss function related to the regularization (from the `loss.out` file). The training RMSEs exhibit oscillations because of the use of mini-batches (with a batch size of 1,000). The test RMSEs closely follow the training RMSEs, which indicates the very good interpolation capability of NEP. In other words, there is no sign of over-fitting. As shown in Ref. 41, a proper regularization is crucial to prevent possible over-fitting in NEP models. Figure 3 shows the results from the `force_test.out` file. We can see that both NEP2 and NEP3 achieve a rather high accuracy here.

B. Comparison of NEP3 with other MLPs

1. A general-purpose silicon data set

We use the general-purpose silicon training data set from Ref. 123 to test convergence with respect to some hyperparameters and compare the results from an implementation of the ACE.⁴⁸ This data set consists of 2,475 structures, including bulk crystal structures, sp^2 bonded structures, dimers, liquid structures, amorphous structures, diamond structures with surfaces or vacancies, and several other defective structures. Every structure has an energy, but not all the structures have virial data. For details on the reference DFT calculations, the reader is referred to Ref. 123.

We use the same cutoff distance of 5 Å for the radial and angular parts and set $n_{\max}^R = n_{\max}^A = N_{\text{bas}}^R = N_{\text{bas}}^A = 10$. We consider using 3-body descriptor components only ($l_{\max}^{3b} = 4$, $l_{\max}^{4b} = 0$, $l_{\max}^{5b} = 0$), using both 3-body and 4-body descriptor components ($l_{\max}^{3b} = 4$, $l_{\max}^{4b} = 2$,

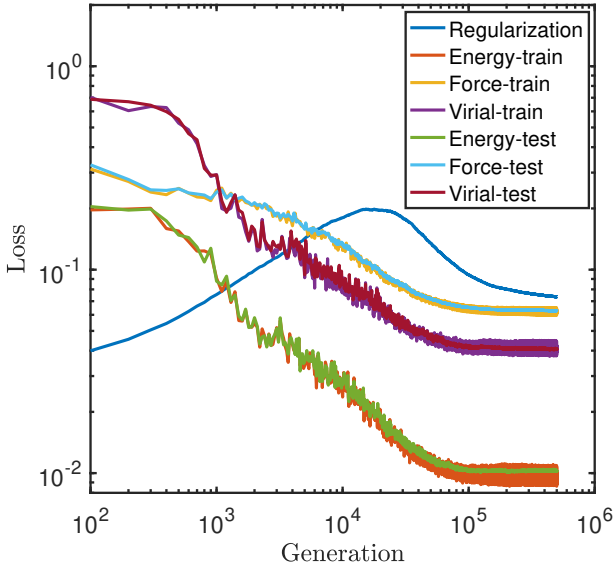


FIG. 2. Evolution of the various terms in the loss function (33) with respect to the generation in the SNES⁶⁸ training algorithm for the MgAlCu training and test data sets.¹²²

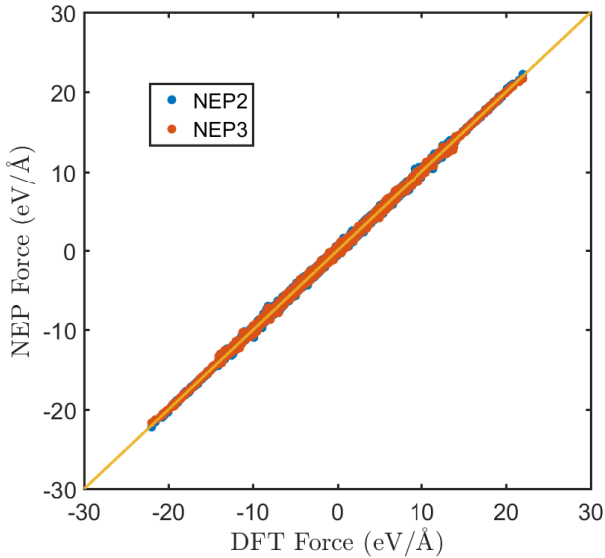


FIG. 3. Forces from NEP2 and NEP3 models against the target DFT values for the MgAlCu test set. The solid line represents the identity function that serves as a guide to the eye.

$l_{\max}^{5b} = 0$), and using up to 5-body descriptor components ($l_{\max}^{3b} = 4$, $l_{\max}^{4b} = 2$, $l_{\max}^{5b} = 1$). Other common hyperparameters are as follows: $\lambda_1 = \lambda_2 = 0.05$, $\lambda_e = 1$, $\lambda_f = 1$, $\lambda_v = 0.1$, $N_{\text{neu}} = 50$, $N_{\text{bat}} = \text{full}$, $N_{\text{pop}} = 50$, and $N_{\text{gen}} = 3 \times 10^5$.

Figure 4 shows the force RMSE versus the computational cost of force evaluation for NEP models and

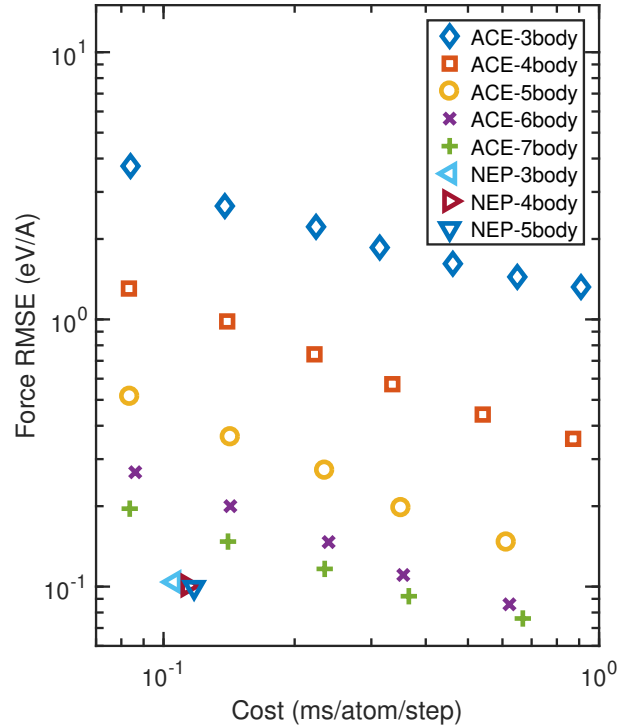


FIG. 4. Force RMSE against computational cost for NEP models for silicon compared to an implementation of the ACE approach (the faster recursive approach as in Ref. 48). A serial C++ implementation of the NEP approach has been tested using an Intel i7-8750H CPU @ 2.2 GHz. For comparison, the ACE potential was implemented in Julia and tested using an Intel i7-7820HQ CPU @ 2.9 GHz.⁴⁸

previous results for an implementation⁴⁸ of the ACE potential⁴⁶ based on linear regression. While the ACE potential shows a strong dependence of the accuracy on the maximum correlation order of the angular descriptor components, our NEP shows a much weaker dependence, although considering 4-body and 5-body correlations indeed helps to increase the accuracy to some degree. With 3-body descriptor components only, the ACE potential has a force RMSE above 1 eV/Å, while the 3-body NEP model already achieves an accuracy of about 0.1 eV/Å. To achieve the same accuracy as the NEP models, one needs to consider up to 6-body descriptor components in the ACE approach and the computational cost is a few times larger than that of the NEP models. The reason for the relative lower cost of the NEP models compared to the ACE model is probably due to the use of a neural network as the regression method instead of linear regression as used in the ACE approach. Using linear regression, the descriptor needs to be rather complete, which can easily lead to more than 10^4 descriptor components,⁴⁸ while the descriptor vector lengths range from 55 to 77 in the present NEP models. With a reduced descriptor length, the completeness⁴⁸ of the descriptor will be

reduced to some degree, but the incompleteness of the descriptor can be (partially) compensated by the neural network and the overall computational cost at a given target accuracy can be lower than using a large number of descriptor components and linear regression. Indeed, within the framework of N -body iterative contraction of equivariants (NICE), nonlinear neural network regression has been shown to be able to achieve higher accuracy than linear regression at least in the limit of large training set size,¹²⁴ using a descriptor up to the same level of the N -body correlation.

2. Azobenzene molecule

Our next example is the largest molecule, azobenzene, in the MD17 data set.¹²⁵ This data set has been revised later¹²⁶ to ensure more strict convergence in the DFT calculations, which is referred to as the revised MD17 data set (rMD17). Here, we use the first train-test split as reported in rMD17,¹²⁶ with 1,000 training structures and 1,000 testing structures randomly chosen from a MD trajectory at 500 K. There are thus 1,000 target energies and 72,000 target force components in the training data set but there are no target virials.

As we have confirmed that adding 4-body and 5-body descriptor components can lead to higher accuracy, here we use $l_{\max}^{3b} = 4$, $l_{\max}^{4b} = 2$, $l_{\max}^{5b} = 1$ and consider different values of the radial function hyperparameters. For simplicity, we set $n_{\max}^R = N_{\text{bas}}^R$ and $n_{\max}^A = N_{\text{bas}}^A$ and consider the following combinations of parameters: $n_{\max}^R = n_{\max}^A = (6, 4)$, $(9, 6)$, $(12, 8)$, and $(15, 10)$. The other hyperparameters are: $r_c^R = 6 \text{ \AA}$, $r_c^A = 4 \text{ \AA}$, $\lambda_1 = \lambda_2 = 0.02$, $\lambda_e = 1$, $\lambda_f = 1$, $\lambda_v = 0$, $N_{\text{neu}} = 50$, $N_{\text{bat}} = \text{full}$, $N_{\text{pop}} = 50$, and $N_{\text{gen}} = 10^6$.

Figure 5 shows the force mean absolute error (MAE) versus the computational cost of force evaluation for our NEP and some other MLPs as reported in Ref. 47, including ANI,¹⁵ GAP,⁸ sGDM²⁴ and a linear-regression based ACE potential⁴⁷ (similar to but not identical to the one in Ref. 48). With increasing n_{\max}^R and n_{\max}^A , both the accuracy and computational cost increase quickly. With $n_{\max}^R = 15$ and $n_{\max}^A = 10$, the NEP approach achieves an accuracy between ANI and GAP, but it is more than one order of magnitude faster than ANI and more than two orders of magnitude faster than GAP. At this level of accuracy, the NEP models are also several times faster than linear-ACE potentials, similar to the case of silicon above (Fig. 4). Similar to the case of silicon, we propose that the superior cost effectiveness of the NEP models compared to the linear-ACE potentials is due to the much smaller descriptor vector size in NEP, which ranges from 32 to 82 in the NEP models, but from 1,700 to 122,000 in the linear-ACE potentials for the test cases in Fig. 5.

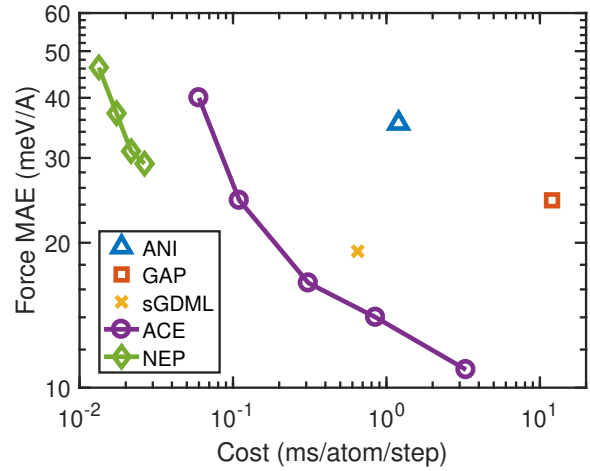


FIG. 5. Force MAE against computational cost from NEP models and several other MLPs for azobenzene as reported in Ref. 47. To be consistent with Ref. 47, we tested our serial C++ code using an Intel Xeon Gold 5218 @ 2.3 GHz.

3. Carbon data set

In this section, we use the training and test data sets for the carbon system with various phases¹⁰ to compare the NEP approach with other MLPs in terms of accuracy, speed, and memory usage. The MLPs to be compared include DP,¹⁷ GAP,⁸ MTP,³⁰ and REANN.⁴⁵ The training data set comprises 4,080 structures in total, including bulk crystal structures, bulk liquid and amorphous structures, amorphous surfaces, and isolated dimer structures. The testing data set comprises 450 structures similar to those in the training data set, but excluding the dimer ones. There are 256,628 and 28,337 atoms in the training and testing data sets, respectively. Each structure has one target energy and each atom has three target force components. Some structures also have target virials. For more details on the data sets, see Ref. 10.

In the case of the NEP approach, we used the NEP3 form and considered two sets of hyperparameters. In the first one, we set $r_c^R = 4.2 \text{ \AA}$, $r_c^A = 3.7 \text{ \AA}$, $n_{\max}^R = N_{\text{bas}}^R = 10$, $n_{\max}^A = N_{\text{bas}}^A = 8$, $l_{\max}^{3b} = 4$, $l_{\max}^{4b} = 2$, $l_{\max}^{5b} = 1$, $\lambda_1 = \lambda_2 = 0.05$, $\lambda_e = 1$, $\lambda_f = 1$, $\lambda_v = 0.1$, $N_{\text{neu}} = 100$, $N_{\text{bat}} = \text{full}$, $N_{\text{pop}} = 50$, and $N_{\text{gen}} = 5 \times 10^5$. This model is labelled “NEP (4.2 Å)” in Table II. In the second one, we make the following changes compared to the first one: $r_c^R = 3.7 \text{ \AA}$, $r_c^A = 3.2 \text{ \AA}$, $l_{\max}^{5b} = 0$, and $N_{\text{neu}} = 50$. This model is labelled “NEP (3.7 Å)” in Table II.

For DP, we used the DEEPM-DKIT package¹⁷ and the smooth edition.¹⁹ We trained two versions of DP, one using the `se_a` descriptor (with a cutoff of 6 Å) only, and the other using a combination of `se_e2_a` (with a cutoff of 6 Å) and `se_e3` (with a cutoff of 3.8 Å). These two versions are labelled “DP (se2)” and “DP(se2+se3)” in Table II, respectively. The size of the embedding net is (25, 50, 100) for the `se_a` and `se_e2_a` descriptors and

TABLE II. Performance comparison between NEP models and other MLPs for the carbon test set from Ref. 10. Energy RMSE ΔE and virial RMSE ΔW are in units of meV/atom while the force RMSE ΔF is in units of meV/Å. Computational speed is measured in atom step/ms. N_{\max} is the maximum number of atoms that can be simulated using one Tesla V100 GPU for the three GPU-accelerated codes. For GAP^{8,10} and MTP^{30,31} 72 Intel Xeon-Gold 6240 CPU cores were used. For DP¹⁷ after compression, NEP and REANN,^{32,45} a 32-GB Tesla V100 GPU was used.

MLP	ΔE	ΔF	ΔW	Speed	N_{\max}
GAP	46	1,100	NA	6.1	NA
DP (se2)	80	1,100	250	290	240×10^3
DP (se2+se3)	44	800	170	150	220×10^3
MTP (4 Å)	36	650	180	110	NA
MTP (5 Å)	35	630	200	61	NA
MTP (6 Å)	35	650	220	27	NA
NEP (4.2 Å)	42	690	160	$3,600$	$4,100 \times 10^3$
NEP (3.7 Å)	44	700	170	$4,600$	$5,800 \times 10^3$
REANN (3 Å)	41	700	NA	280	290×10^3
REANN (4 Å)	31	640	NA	170	180×10^3
REANN (6 Å)	28	670	NA	62	64×10^3

(20, 40, 80) for the `se_e3` descriptor, and the size of the fitting net is (240, 240, 240). The learning rate decreases exponentially from 10^{-3} to 10^{-8} . The weighting parameters for energy, force, and virial have a starting value of 0.02, 1,000, and 0.01, respectively, which are linearly changed to 1, 1, and 0.1 during the training process. The number of training steps is 10^7 , which is sufficiently large.

For GAP,^{8,10} we directly took the results from Ref. 10. The n_{\max} and l_{\max} for the smooth overlap of atomic positions (SOAP) descriptor were both set to 8.¹⁰ There were also separate low-dimensional 2-body and 3-body components in this GAP.¹⁰

For MTP,³⁰ we used the MLIP package.³¹ The descriptor level of the MTP is set to 22. We considered three cutoff distances: 4 Å, 5 Å, and 6 Å, labelled “MTP (4 Å)”, “MTP (5 Å)”, and “MTP (6 Å)”, respectively, in Table II.

For REANN,⁴⁵ we used the REANN package.³² We considered three cutoff distances: 3 Å, 4 Å, and 6 Å, labelled “REANN (3 Å)”, “REANN (4 Å)”, and “REANN (6 Å)”, respectively, in Table II. The weighting parameter for energy is kept at 1 and that for force is decreased from 10 to 0.5 during the training process. A batch-size of 32 is used (we have tried to use a larger batch-size and it turned out to exceed the memory limit of a 32-GB V100). The sizes of the neural network for the atom energy and the orbital coefficients are both (64, 64). The learning rate decreases exponentially from 10^{-3} to 10^{-7} . The number of training epochs is 10^4 .

For all MLPs, we list the RMSEs for energies, forces, and virials (calculated from 6 independent components) in Table II. The MTP and REANN models show the best accuracy in energies and forces, and GAP and DP the worst. The accuracy of the NEP models is close to those

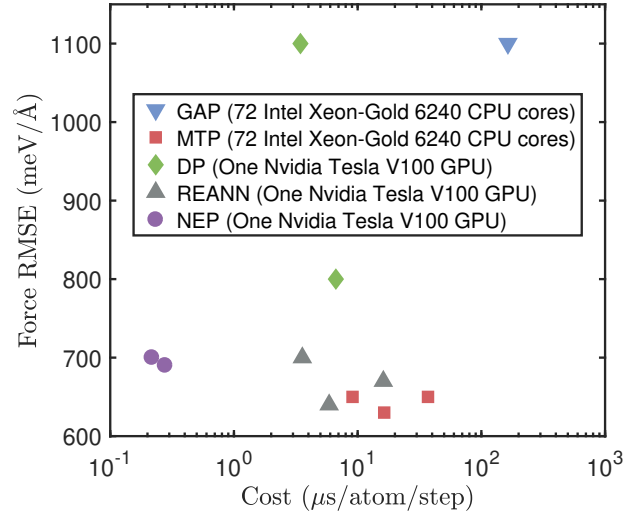


FIG. 6. Force RMSE against computational cost from NEP models and other MLPs for the carbon data set from Ref. 10.

of MTP and REANN. The virial RMSE is missing for GAP as no predicted virial data have been provided.¹⁰ It is also missing for REANN because the virial has not been formulated in this MLP. For the MLPs with available virial data, the NEP models achieve the highest accuracy. Therefore, we can say that the NEP models at least have an above-average accuracy for this carbon data set.

With the accuracy comparison results in mind, we next compare the computational performance in realistic atomistic simulations. Here, we run MD simulations for a cubic cell of diamond in the isothermal ensemble at 300 K for 100 steps and output some basic thermodynamic properties every 10 steps. Based on the MD simulations, we measure the computational speed as the product of the number of atoms and the number of steps divided by the total wall time used. Three of the MLPs (DP, REANN, NEP) have been implemented on GPUs and we thus use an Nvidia Tesla V100 GPU for the test. For the other two MLPs for which there are only CPU versions available (GAP and MTP) we use 72 Intel Xeon-Gold 6240 cores. The CPU and GPU resources might have unequal financial costs, but one can make suitable conversions of the results presented here to other computational environments. For the CPU-based MLPs, MTP shows much higher computational speed than GAP, which is consistent with previous tests.³⁰ For the GPU-based MLPs, DP (after model compression) and REANN have comparable speed, while the NEP models are more than one order of magnitude faster. Figure 6 shows that the NEP models substantially lower the Pareto front of accuracy-versus-cost that can be achieved by the other MLPs.

Interestingly, the GPU memory usage seems to be correlated to the computational speed: the maximum number of atoms N_{\max} that can be simulated using one Tesla

V100 GPU is roughly proportional to the computational speed. This comparison highlights the superior computational performance of the NEP approach as implemented in GPUMD in terms of both computational speed and memory efficiency, which is crucial for tackling challenging applications that require large-scale and long-time atomistic simulations.

IV. ACTIVE LEARNING BASED ON THE LATENT SPACE

Apart from regression accuracy and MD speed, training data preparation is an important aspect of MLPs. Because quantum-mechanical calculations are usually time consuming, it is desirable to construct a minimal training data set for a given application. One strategy for achieving this is to use active learning (AL), which uses query criteria to determine whether or not a new training sample should be included into an existing training set to improve the model accuracy and generalization capability. Many AL schemes have been proposed for MLPs, including the ensemble (or query-by-committee) method,^{127–129} the dropout method,¹³⁰ methods based on feature-space distance measuring¹³¹ and entropy maximization in the descriptor space,¹³² and methods based on optimal design.^{133,134} Here, we propose an AL scheme based on the latent space of a pre-trained NEP model. This AL scheme has been inspired by the work of Janet *et al.*,¹³⁵ who have shown that distance in the latent space provides a good quantitative uncertainty metric to be used in an AL scheme.

There is no unique definition of the latent space. Here, we define it as an N_{neu} -dimensional space spanned by the vectors whose components are the product of the states of the hidden-layer neurons and the connection weights between them and the output layer. To compute the latent-space vector for a structure, one must train a NEP model first, but this can be achieved by using a small initial training data set. Then one can use the pre-trained NEP model to compute the latent-space vectors for many structures, either those in the training data set or new ones that have no target values (energy, forces, and virials) yet. This allows one to generate target values (via quantum-mechanical calculations) for a number of structures that have relatively large distances to existing points in the latent space. This procedure can be iterated by updating the training data set and the NEP model in alternating fashion. During this process, the existing NEP model can be used to create the new structures to be examined, using various sampling techniques in atomistic simulations.

We take the carbon data set as a concrete example to illustrate the idea outlined above. To this end, suppose we only have 200 structures randomly selected out of the 4,080 ones in the original training data set. We first train an initial NEP using these 200 structures, adopting the same hyperparameters as used for the NEP (4.2 Å) model

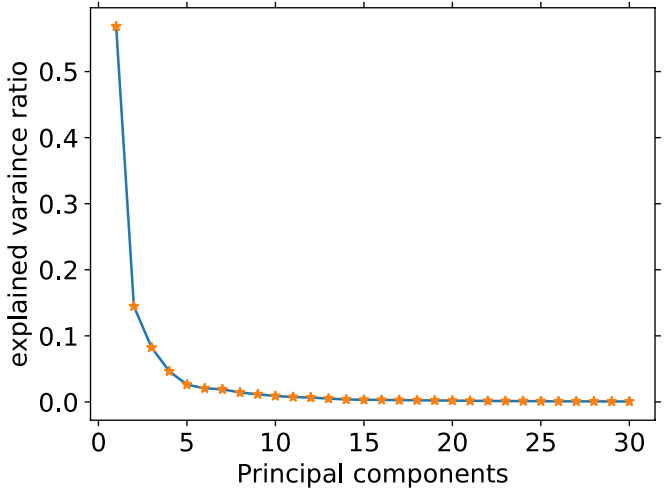


FIG. 7. Normalized explained variance ratio of the first 30 principal components calculated from the 4,080 structures in the original training data set¹⁰ based on the initial NEP model trained using 200 structures.

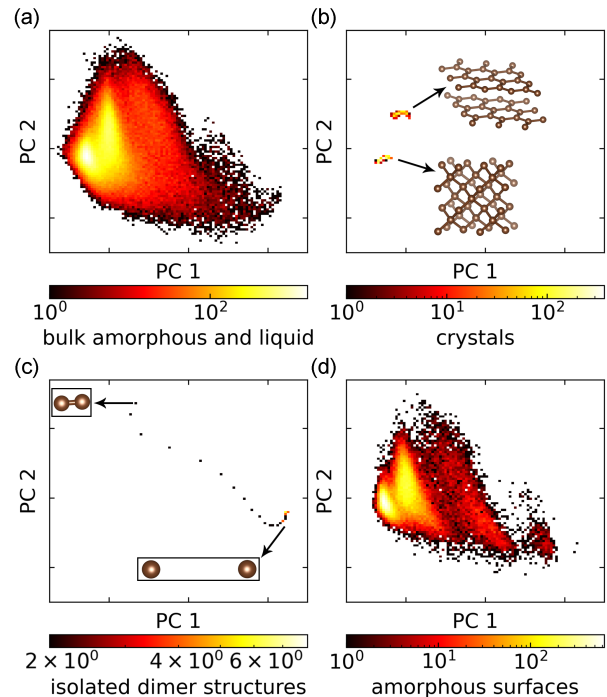


FIG. 8. Distribution of the 4,080 carbon structures in the full training data set¹⁰ in the 2D principal component (PC) space (spanned by PC 1 and PC 2) as reduced from the latent space that was constructed using the initial NEP model trained using 200 structures. (a) bulk amorphous/liquid structures, (b) crystals including sp^2 graphite and sp^3 diamond structures, (c) dimers, and (d) surface amorphous structures. The color bar represents the density of structures in the 2D PC space.

in Table II. Assuming that we have obtained the remaining structures as in the original training data set by various means, we then compute the latent space vectors for all the 4,080 structures. One can define a distance in the high-dimensional latent space, but it turns out that the high dimension can be effectively reduced using principal component (PC) analysis. The explained variance ratios of the first 30 PCs are shown in Fig. 7. The first two leading PCs contribute more than 70% to the total dimensions, allowing us to visualize the distribution of structures in a 2D PC space, as shown in Fig. 8. It can be seen that both dimers and crystals (with or without defects) occupy a small area in the PC space. On the other hand, both bulk and surface amorphous/liquid structures occupy large areas that are almost overlapping. Furthermore, the high density part in Fig. 8a indicates that there are relatively more bulk amorphous and liquid structures in the full training data set.

Based on these observations, we construct a new training data set which includes all the dimers (30 in total) and crystals (356 in total), and 400 bulk amorphous/liquid structures. Using these 786 structures, we train a new NEP model using the same hyperparameters as for the NEP (4.2 Å) model in Sect. III B 3). The energy, force, and virial RMSEs from this NEP model are 45 meV/atom, 700 meV/Å, and 190 meV/atom, respectively, for the same test data set as used in Sect. III B 3), which are very close to those for the NEP model trained using the full training data set. Figure 9 shows that the AL-based NEP model indeed performs very well in the various predicted values. The force RMSE (660 meV/Å) for the AL-based NEP model is only slightly higher than that for the NEP model trained using the full training data set (650 meV/Å). This is a notable result since we have not included a single surface amorphous structure into the training data set for the AL-based NEP model. This shows that the distance in the latent space (and the reduced PC space) indeed provides a reliable metric for selecting new samples for the construction of accurate and transferable MLPs. The present results also indicate that the NEP approach is quite data efficient, which we attribute to the relatively simple neural-network model and the inclusion of regularization terms in the loss function. As a further demonstration of the reliability of the AL-based NEP model, we show in Sect. V below that it performs equally well as the NEP model trained against the full training data set in an MD simulation covering a large range of temperatures.

V. EXAMPLES FOR APPLICATIONS OF NEP MODELS

In this section, we demonstrate the application of NEP models in atomistic simulations. To this end, we employ the NEP (4.2 Å) model from Table II, if not stated otherwise.

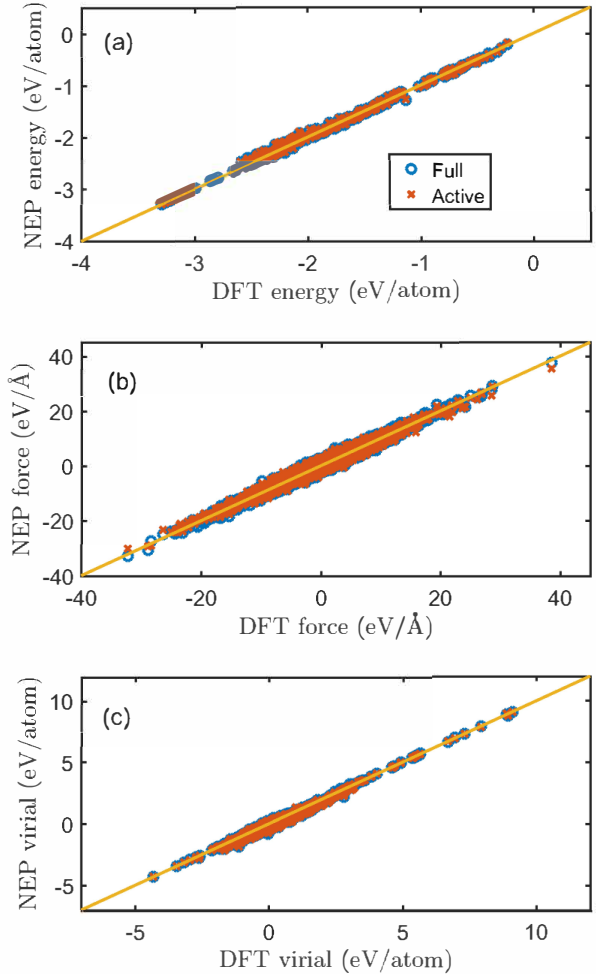


FIG. 9. (a) Energy, (b) force, and (c) virial values from the NEP models for carbon constructed using the full training data set (4,080 structures, labelled “Full”) and the training data set constructed based on active learning (786 structures, labelled “Active”), in comparison to the DFT reference data for the test data set (450 structures).¹⁰

A. Lattice constant

We begin with a simple static calculation and determine the zero-temperature lattice constant of diamond by calculating a cohesive energy curve. The `run.in` input file reads:

```
potential potentials/nep/C_2022_NEPE3.txt 0
compute_cohesive 0.98 1.03 51
```

The `potential` keyword specifies the NEP model to be used and the `compute_cohesive` keyword is used to invoke the cohesive energy calculation. The lattice constant thus obtained is 3.530 Å, which is very close to the DFT reference value obtained using the local density approximation (LDA), see Table III.

TABLE III. Structural and elastic properties of diamond from the NEP (4.2 Å) model in comparison to GAP and DFT-LDA results.¹⁰

	DFT-LDA	GAP	NEP (4.2 Å)
a (Å)	3.532	3.539	3.530
C_{11} (GPa)	1, 101	1, 090	1, 134
C_{12} (GPa)	148	112	153
C_{44} (GPa)	592	594	605

B. Elastic constants

Next we compute the zero-temperature elastic constants, for which the `run.in` input file reads:

```
potential potentials/nep/C_2022_NEPE3.txt 0
compute_elastic 0.01 cubic
```

Here, the `compute_elastic` keyword is used to initiate the calculation of the three independent elastic constant components (C_{11} , C_{12} , and C_{44}) using the energy-strain relation with $\pm 1\%$ strain values. The computed elastic constants are presented in Table III. The elastic constants from the NEP model are within 4% of the reference DFT-LDA values. For comparison, the C_{12} value from GAP is about 24% smaller than the reference DFT-LDA value. We note that including virial information during training is crucial for obtaining accurate elastic properties, as can be seen from Fig. 10. In other words, fitting to energy and force data alone does not guarantee an accurate description of virials. Since the calculation of the heat current involves virial terms, see Eq. (25), this is also important for heat transport applications, as has already been pointed out by Shimamura *et al.*¹³⁶

C. Tensile loading of diamond

All the calculations above are static ones at zero temperature. Here, we use MD simulations to study the fracture of diamond under uniaxial tensile loading. The `run.in` input file reads:

```
potential potentials/nep/C_2022_NEPE3.txt 0
velocity 300

ensemble npt_ber 300 300 100 0 0 0
          1000 1000 1000 1000
time_step 1
run      100000

ensemble      npt_scr 300 300 100 0 0 0
                  1000 1000 1000 1000
deform      1.42e-5 0 0 1
dump_thermo 100
dump_position 10000
run        5000000
```

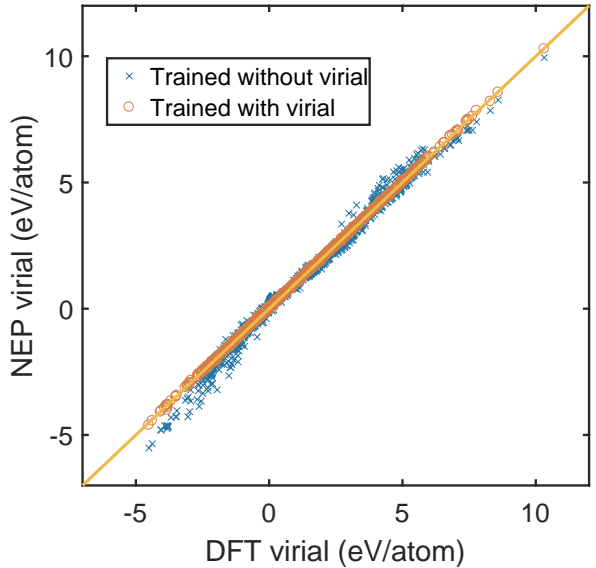


FIG. 10. Virial values from the NEP models in comparison with DFT-LDA data for the carbon data set.¹⁰

The simulated model is a periodic supercell comprising of $5 \times 5 \times 40$ conventional cubic unit cells and hence 8,000 atoms. We first equilibrate the system at 300 K and zero pressure using the NPT ensemble via the Berendsen thermostat and barostat⁷⁵ for 100 ps. Then we switch to the Bussi-Donadio-Parrinello thermostat⁷⁹ and the Bernetti-Bussi barostat⁸² in the production stage, deforming the simulation box in the z direction with a strain rate of 1×10^8 /s for 5 ns up to a strain of 50%, while the pressures in the x and y directions are set to zero. Based on the output thermodynamic quantities and trajectory, we can obtain the stress-strain relation as shown in Fig. 11 and identify a snapshot of the fracture process as shown in Fig. 12. The fracture is brittle with a fracture strength of about 200 GPa at a strain of about 29%. We note that more independent simulations are needed to obtain statistically meaningful results beyond the current demonstration.

D. Quenching

The carbon data set¹⁰ is particularly suitable for studying liquid and amorphous carbon.^{10,137,138} In this example, we use a melt-quench-anneal protocol similar to that used in Ref. 10 (but with ten times longer simulation time for the relaxation at each temperature and an extra relaxation at 1000 K) to generate amorphous carbon. The `run.in` file reads:

```
potential potentials/nep/C_2022_NEPE3.txt 0
velocity 9000

ensemble      nvt_lan 9000 9000 100
```

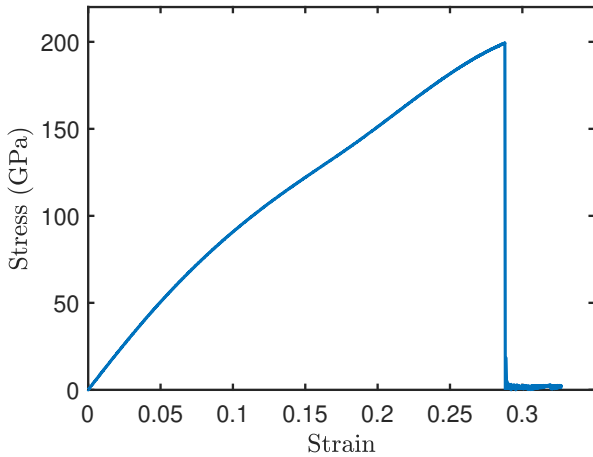


FIG. 11. Stress-strain relation from a uniaxial tensile loading simulation of diamond using the NEP (4.2 Å) model for carbon.

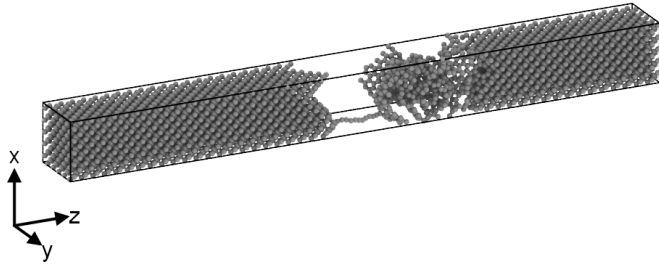


FIG. 12. A snapshot sampled during the fracture process under uniaxial tensile loading.

time_step	1
dump_thermo	10
dump_position	1000
run	30000
ensemble	nvt_lan 5000 5000 100
dump_thermo	10
dump_position	1000
run	30000
ensemble	nvt_lan 5000 1000 100
dump_thermo	10
dump_position	100
run	500
ensemble	nvt_lan 1000 1000 100
dump_thermo	10
dump_position	1000
run	30000
ensemble	nvt_lan 300 300 100
dump_thermo	10
dump_position	1000

run	30000
-----	-------

The initial simulation model is a cubic diamond supercell containing 64,000 atoms with a mass density of 3.0 g/cm³. The system is first quickly melted at 9.000 K and then relaxed at 5.000 K, followed by a quick quenching from 5.000 K to 1.000 K and further relaxation at 1.000 K and 300 K. Here, the Langevin thermostat⁸⁰ is used to control the temperature. The evolution of temperature and the ratio of sp³-bonded atoms as a function of simulation time are presented in Fig. 13a-b. The radial and angular distribution functions $g(r)$ and $g(\theta)$ at 5.000 K and 300 K in Fig. 13(c)-(d) show that the system is in liquid and amorphous-solid states, respectively. We also performed the same MD simulation using the NEP model trained with the AL scheme in Sect. IV and we can see that it gives almost identical results as those from the NEP model trained using the full training data set. This further demonstrates the effectiveness of our AL scheme based on the latent space.

E. Density of states and heat capacity of amorphous carbon

After obtaining amorphous carbon structures, we further study their thermal properties. In this example, we calculate the vibrational density of states (VDOS) for an amorphous carbon structure and then obtain the heat capacity with quantum corrections. The `run.in` file reads:

potential	potentials/nep/C_2022_NE3.txt	0
velocity	300	
ensemble	nvt_ber	300 300 100
time_step	1	
run	10000	
ensemble	nve	
compute_dos	5 200 400	
run	100000	

The VDOS $\rho(\omega)$ is calculated from the velocity autocorrelation function (VACF).¹³⁹ The VACF and VDOS are normalized to $3N$, where N is the number of atoms. The per-atom heat capacity with quantum corrections at the temperature T is then calculated as

$$C(T) = \frac{1}{N} \int_0^\infty \frac{d\omega}{2\pi} \rho(\omega) \frac{x^2 e^x}{(e^x - 1)^2}, \quad (34)$$

where $x = \hbar\omega/k_B T$ is the ratio of the vibrational energy $\hbar\omega$ and the thermal energy $k_B T$.

F. Thermal conductivity of amorphous carbon

In this last example, we calculate the thermal conductivity of our amorphous carbon sample using the

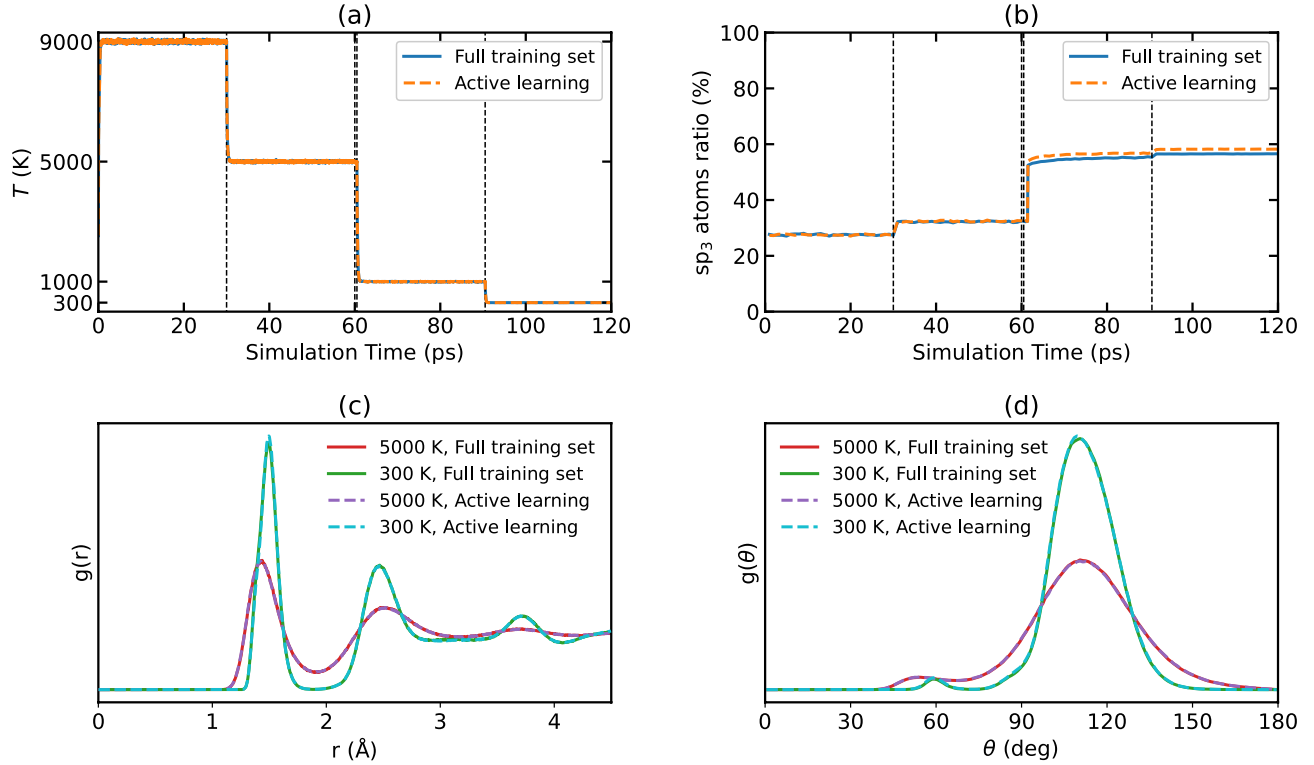


FIG. 13. (a) Temperature and (b) ratio of sp^3 bonded atoms as a function of simulation time as obtained using the NEP (4.2 Å) model. (c) Radial and (d) angular distribution functions at 5.000 K and 300 K.

HNEMD method and the related spectral decomposition method.^{61,87} The `run.in` file reads:

```

potential      potentials/nep/C_2022_NEP3.txt 0
velocity      300

ensemble      nvt_nhc 300 300 100
time_step     1
run          100000

ensemble      nvt_nhc 300 300 100
compute_hnemd 1000 0 0 2e-4
compute_shc   5 200 2 500 400
run          2000000

```

Thermal conductivity calculations usually require a lot of data to reduce the statistical uncertainty. To this end, we perform a number of independent runs using the above inputs. In GPUMD, the velocities are automatically initialized with different pseudo-random number seeds for different runs. Using the efficient HNEMD method, 5 independent runs (each with a production time of 2 ns) are sufficient to achieve high accuracy (small error bounds), as can be seen from Fig. 15a. The thermal conductivity of the amorphous carbon structure (with a mass density of 3.0 g/cm³) at 300 K is determined to be 5.1 ± 0.1 W/(m K), where the statistical error is calculated as the standard error.¹⁴⁰ The thermal conductivity

calculated in this way is the classical value. For disordered materials, the thermal conductivity can be quantum corrected in a way similar to the quantum correction of the heat capacity.¹⁴¹ To achieve this, we first calculate the classical spectral thermal conductivity^{61,87} $\kappa^c(\omega)$ and include quantum corrections to obtain $\kappa^q(\omega)$ as follows:

$$\kappa^q(\omega) = \kappa^c(\omega) \frac{x^2 e^x}{(e^x - 1)^2}, \quad (35)$$

where $x = \hbar\omega/k_B T$. Both $\kappa^c(\omega)$ and $\kappa^q(\omega)$ at 300 K are shown in Fig. 15b. The quantum-corrected thermal conductivity at 300 K is 3.2 ± 0.1 W/(m K). A more systematic investigation of the thermal transport properties in disordered carbon systems will be presented elsewhere.

VI. INTERFACE TO OTHER CODES

A. The `gpyumd` package

To help GPUMD users generate input and process output files, we have developed a Python interface implemented in the `GPyUMD` package. Reading, preparing, and writing `xyz.in` files is facilitated by the `GpumdAtoms` class. This class extends the `Atoms` class from the popular Atomic Simulation Environment (ASE) Python

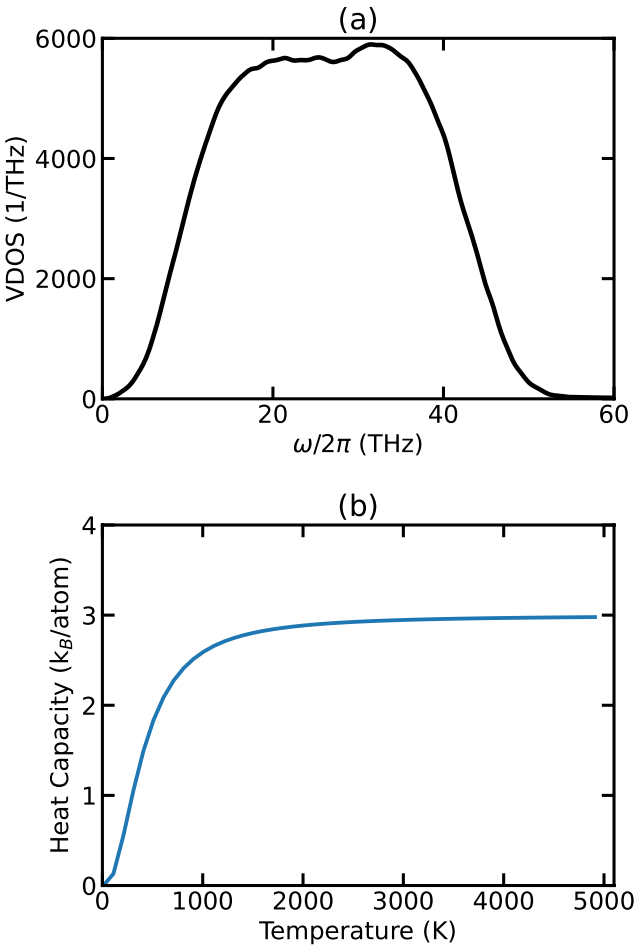


FIG. 14. (a) VDOS of amorphous carbon with a density of 3.0 g/cm^3 at 300 K as obtained using the NEP (4.2 \AA) model. (b) Heat capacity with quantum corrections calculated from the VDOS via Eq. (34).

package¹⁴² to include GPUMD-specific properties. A simple example of writing an `xyz.in` file is as follows:

```
from ase.lattice.cubic import Diamond
from gpyumd.atoms import GpumdAtoms

Si = GpumdAtoms(Diamond("Si", size=(10,10,10)))
Si.set_max_neighbors(4)
Si.set_cutoff(3)
Si.write_gpumd()
```

The `GpumdAtoms` class also supports adding grouping methods, sorting atoms by group or type, generating `basis.in` and `kpoints.in` files for phonon calculations, and more.

The GPYUMD package also has a `Simulation` class that can be used to generate valid `run.in` files. To do so, in addition to checking each keyword parameter, it verifies that group selections in each keyword, atom types in potential definitions, and atom ordering in the `xyz.in` file

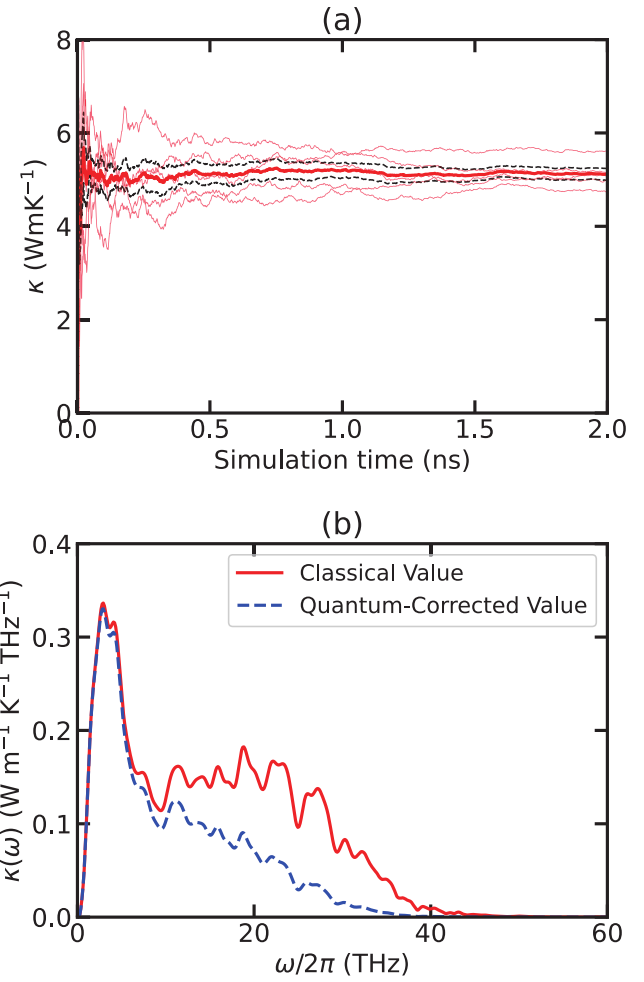


FIG. 15. (a) Thermal conductivity of amorphous carbon as calculated from the HNEMD method using the NEP (4.2 \AA) model. The thin solid lines are from 5 independent runs and the thick solid line is their average. The dashed lines represent the error bounds. (b) Classical and quantum-corrected spectral thermal conductivity as a function of the vibrational frequency.

are consistent. As a simple demonstration, continuing from our previous code snippet, we can create a simple `run.in` file as follows:

```
import gpyumd.keyword as kwd
from gpyumd.sim import Simulation

sim = Simulation(Si)
run = sim.add_run()
keywords = [
    kwd.Velocity(initial_temperature=300),
    kwd.TimeStep(dt_in_fs=1),
    kwd.Ensemble(ensemble_method='nve'),
    kwd.DumpThermo(interval=1000),
    kwd.RunKeyword(number_of_steps=1e5)]

[run.add_keyword(x) for x in keywords]
```

```

potential = kwd.Potential(filename='Si.txt',
                           symbols=['Si'])
sim.add_potential(potential)
sim.create_simulation()

```

The output files of GPUMD can be read and processed using simple GPYUMD functions such as `load_thermo()` for the `thermo.out` file, `load_hac()` for the `hac.out` file, etc. These functions return the data in convenient formats for data exploration in interactive environments such as Jupyter Notebooks.

B. The calorine package

To provide a deeper integration of GPUMD within a Python workflow, we also provide the Python package CALORINE. This section outlines the functionality of this package.

1. ASE calculator

The CALORINE package extends the functionality of ASE, implementing an `ASE Calculator` class, which lets users calculate energies, forces, and stresses with a NEP model directly from Python. Under the hood, this calculator writes and reads the GPUMD input and output files. A minimal script reads as follows:

```

from calorine.ase_calculator import GPUMD_NEPE
from ase.build import bulk

calculator = GPUMD_NEPE('nep.txt')
atoms = bulk('Au', a=4.1)
atoms.set_calculator(calculator)
e = atoms.get_potential_energy()

```

This approach can, for example, greatly simplify the calculation of a large number of pre-defined structures, and provides access to various complex structural relaxation schemes available in ASE.

2. Pybind11 interface

CALORINE also interfaces directly to GPUMD using a PYBIND11 C++ interface. This enables easy access to the data structures associated with the NEP implementation in GPUMD. At the moment the interface exposes a function for calculating the descriptors for an ASE `Atoms` object, but this can be easily extended.

An example script for accessing the GPUMD descriptors for a structure is given below.

```

from ase import Atoms
from calorine.nepy.nep import get_descriptors

```

```

CO = Atoms(
    'CO',
    positions=[(0, 0, 0), (0, 0.0, 1.1)]
)
descriptors_CO = get_descriptors(CO)

```

VII. SUMMARY AND CONCLUSIONS

In summary, we have presented the various features of the open-source GPUMD package, with a focus on recent developments that have enabled the generation and use of accurate and efficient NEP MLPs.^{41,42} Two improvements on the atomic-environment descriptor have been introduced: one is to change the radial functions from Chebyshev basis functions to linear combinations of the basis functions, and the other is to extend the angular descriptor components by considering some 4-body and 5-body contributions as in the ACE approach.⁴⁶ Both of these extensions are shown to improve the accuracy of NEP models further.

We have used a diverse set of materials to demonstrate that the NEP approach can achieve an above-average accuracy compared to many other state-of-the-art MLPs. In addition, NEP models can achieve a far superior computational efficiency: typical NEP models are more than one order of magnitude faster than other MLPs and similarly more memory efficient. The high efficiency of NEP models originates from many aspects, including a reasonably small descriptor dimension (usually smaller than 100) combined with a simple neural network model with a single hidden layer, carefully derived expressions of the descriptor components, a balanced choice of the radial and angular cutoff distances, and finally a carefully optimized GPU implementation. We present our algorithms in detail in Appendix B. The latent space in the simple neural network model of NEP models also allows us to construct an effective AL scheme that can be used to greatly reduce the computational efforts in the preparation of training data.

Apart from being highly efficient, GPUMD is also user-friendly. It can both be used as a standalone package and be integrated with other packages such as ASE¹⁴² via the GPYUMD and CALORINE Python packages. The use of an efficient derivative-free optimization algorithm (SNES) greatly simplifies the implementation and excludes the dependence of GPUMD on any third-party machine-learning libraries, making the installation of GPUMD effortless.

Finally, the NEP models trained using the `nep` executable can be directly used by the `gpumd` executable to perform atomistic simulations of various materials properties. To demonstrate the range of properties, length and time scales that can be accessed via this approach, we have presented a series of examples using a NEP model trained using a standard carbon data set.¹⁰

One of the disadvantages of GPUMD is that it is still

not very feature-rich (as compared to similar packages such as LAMMPS⁷¹). However, its open-source nature and the well-designed GPU-acceleration framework have been attracting more and more developers with diverse backgrounds who are enriching the features of GPUMD at a fast pace.

Data availability

The training and testing results using the various MLPs as presented in Sect. III and Sect. IV are freely available via Zenodo.¹⁴³ The input and output files for the GPUMD examples presented in Sect. V are included in the GPUMD package (<https://github.com/brucefan1983/GPUMD>).

Code availability

The source code of GPUMD and CALORINE is maintained via git and available at <https://github.com/brucefan1983/GPUMD> and <https://gitlab.com/materials-modeling/calorine>. The respective documentation pages can be found at <https://gpumd.zheyongfan.org/> and calorine.materialsmodeling.org/. The latent-space-based active learning analyses have been facilitated by the PyNEP package available at <https://github.com/bigd4/PyNEP>. The source code and documentation of GPyUMD will be published soon.

ACKNOWLEDGMENTS

Z.F. acknowledges support from the National Natural Science Foundation of China (NSFC) (No. 11974059). Y.W., K.S., J.L., and H.D. acknowledge the support from the National Key Research and Development Program of China (2018YFB0704300). The work at Nanjing University (J.J.W, Y.W., J.S.) is partially supported from the NSFC (grant nos. 12125404, 11974162, and 11834006), and the Fundamental Research Funds for the Central Universities. The calculations performed in Nanjing University were carried out using supercomputers at the High Performance Computing Center of Collaborative Innovation Center of Advanced Microstructures, the high-performance supercomputing center of Nanjing University. P.Y. and Z.Z. acknowledge support from the NSFC (No. 11932005). T.A-N. has been supported in part by the Academy of Finland through its QTF Centre of Excellence program (No. 312298) and Technology Industries of Finland Centennial Foundation Future Makers grant. Z.Z. and Y.C. are grateful for the research computing facilities offered by ITS, HKU, J.M.R., E.L., and P.E. acknowledge support from the Swedish Research Council (2018-06482, 2020-04935, 2021-05072) and the Swedish Foundation for Strategic Research (SSF) via the SwedNess program (GSn15-0008) as well as computational resources provided by the Swedish National Infrastructure for Computing (SNIC) at NSC, C3SE, and PDC partially funded by the Swedish Research Council

(2018-05973).

Appendix A: Some derivations on the heat current expressions

Here we show that the heat current expressions for the multi-body potentials as considered in Ref. 67 are special cases of the general expressions in our formulation. Without loss of generality, we take the 3-body potential as an example to show this.

Using the chain rule, we first rewrite Eq. (27) as

$$\mathbf{J} = - \sum_i \sum_{j \neq i} \mathbf{r}_{ij} \frac{\partial U_i}{\partial \mathbf{r}_j} \cdot \mathbf{v}_j. \quad (\text{A1})$$

Boone *et al.*⁶⁷ considered explicit m -body potentials ($m = 2, 3, 4$) that are usually used in topological force fields for organics. For the 3-body potential considered therein, the site potential U_i of atom i is taken as the average of the potentials of the triplets it belongs to (the first index denotes the central atom of a triplet):

$$U_i = \frac{1}{3} \sum_{k \neq i} \sum_{l \neq i} (U_{ikl} + U_{kli} + U_{lik}). \quad (\text{A2})$$

Substituting Eq. (A2) into Eq. (A1), we have

$$\mathbf{J} = - \frac{1}{3} \sum_i \sum_{j \neq i} \sum_{k \neq i} \sum_{l \neq i} \mathbf{r}_{ij} \frac{\partial (U_{ikl} + U_{kli} + U_{lik})}{\partial \mathbf{r}_j} \cdot \mathbf{v}_j. \quad (\text{A3})$$

Note that j cannot be i but could be k or l and we thus have

$$\frac{\partial U_{ikl}}{\partial \mathbf{r}_j} = \delta_{jk} \frac{\partial U_{ijl}}{\partial \mathbf{r}_j} + \delta_{jl} \frac{\partial U_{ikj}}{\partial \mathbf{r}_j} \quad (\text{A4})$$

and similar expressions for $\frac{\partial U_{kli}}{\partial \mathbf{r}_j}$ and $\frac{\partial U_{lik}}{\partial \mathbf{r}_j}$. Following Boone *et al.*⁶⁷ we can define

$$\mathbf{F}_j^{ijl} \equiv - \frac{\partial U_{ijl}}{\partial \mathbf{r}_j}. \quad (\text{A5})$$

as the force acting on atom j from the triplet ijl . Then we can write Eq. (A3) as

$$\mathbf{J} = \frac{1}{3} \sum_i \sum_{j \neq i} \sum_{k \neq i} \mathbf{r}_{ij} \left(\mathbf{F}_j^{ijk} + \mathbf{F}_j^{ikj} + \mathbf{F}_j^{jki} + \mathbf{F}_j^{kji} + \mathbf{F}_j^{jik} + \mathbf{F}_j^{kij} \right) \cdot \mathbf{v}_j. \quad (\text{A6})$$

By manipulating the dummy indices in the summation, it can be written as

$$\mathbf{J} = \frac{1}{3} \sum_i \sum_{j \neq i} \sum_{k \neq i} (\mathbf{r}_{ji} + \mathbf{r}_{ki}) \mathbf{F}_i^{ijk} \cdot \mathbf{v}_i + (\mathbf{r}_{ij} + \mathbf{r}_{kj}) \mathbf{F}_j^{ijk} \cdot \mathbf{v}_j + (\mathbf{r}_{ik} + \mathbf{r}_{jk}) \mathbf{F}_k^{ijk} \cdot \mathbf{v}_k, \quad (\text{A7})$$

which corresponds to Eq. (18d) in Ref. 67.

Appendix B: Algorithms

In this Appendix, we present the complete algorithms for evaluating the NEP energy, force, and virial expressions as implemented in GPUMD. First we list all the relevant quantities:

1. N is the total number of atoms.
2. NN_i^R is the number of neighbors of atom i for the radial descriptor components.
3. NN_i^A is the number of neighbors of atom i for the angular descriptor components.
4. NL_{im}^R is the index of the m -th neighbor of atom i for the radial descriptor components.
5. NL_{im}^A is the index of the m -th neighbor of atom i for the angular descriptor components.
6. $\{\mathbf{r}_i\}_{i=0}^{N-1}$ are the atom positions.
7. $\{U_i\}_{i=0}^{N-1}$ are the site energies.
8. $\{\partial U_i / \partial q_\nu^i\}_{i=0}^{N-1}$ are the derivatives of the site energies with respect to the descriptor components.
9. $\{\partial U_i / \partial \mathbf{r}_{ij}\}_{i=0}^{N-1}$ are the partial forces.
10. $\{\mathbf{F}_i\}_{i=0}^{N-1}$ are the forces on the atoms.
11. $\{\mathbf{W}_i\}_{i=0}^{N-1}$ are the virials on the atoms.

1. Application of the neural network

We use a simple feedforward neural network with a single hidden layer. We have done extensive tests and found that a single hidden layer is sufficient to achieve high accuracy for NEP models and using more hidden layers only reduces computational performance without a corresponding improvement in model accuracy. Using a single hidden layer, many variables can be defined as registers instead of global memory or local memory in the CUDA kernel, which are much more expensive to access. Therefore, using a single hidden layer can achieve a significantly higher computational performance in the parallelism scheme we adopted.

Listing 1. The function applying the feedforward neural network to the input descriptor vector to obtain the site energy of an atom and the derivative of the energy with respect to the descriptor components.

```

1  __device__ void apply_ann(
2      const int N_des,
3      const int N_neu,
4      const float* w0,
5      const float* b0,
6      const float* w1,
```

```

7      const float* b1,
8      const float* q,
9      float& energy,
10     float* energy_derivative)
11 {
12     for (int n = 0; n < N_neu; ++n) {
13         float w0_times_q = 0.0f;
14         for (int d = 0; d < N_des; ++d) {
15             w0_times_q += w0[n*N_des+d] * q[d];
16         }
17         float x1 = tanh(w0_times_q - b0[n]);
18         float tanh_der = 1.0f - x1 * x1;
19         energy += w1[n] * x1;
20         for (int d = 0; d < N_des; ++d) {
21             float y1 = tanh_der * w0[n*N_des+d];
22             energy_derivative[d] += w1[n] * y1;
23         }
24     }
25     energy -= b1[0];
26 }
```

The complete `__device__` function applying the neural network is presented in Listing 1. For the inputs, N_{des} is the dimension N_{des} of the descriptor vector, N_{neu} is the number of neurons N_{neu} in the hidden layer, $w0$ is the weight matrix $\mathbf{w}^{(0)}$, $w1$ is the weight vector $\mathbf{w}^{(1)}$, $b0$ is the bias vector $\mathbf{b}^{(0)}$ in the hidden layer, $b1$ is the bias $b^{(1)}$ in the output node, and q is the descriptor vector \mathbf{q}^i . For the outputs, `energy` is the site energy U_i and `energy_derivative` is the derivative of the site energy with respect to the descriptor components $\partial U_i / \partial q_\nu^i$. Note that we do not need to calculate the derivative of the energy (and other related quantities such as force and virial) with respect to the neural-network parameters, as required in the conventional gradient-descent approach. In our evolutionary algorithm approach, there is no need to calculate the derivative of the loss function with respect to any parameters. Therefore, our implementation is very simple regarding the neural network part and particularly, we do not make GPUMD dependent on any third-party packages. This makes the installation of GPUMD very simple and straightforward.

2. Energy and derivative of energy with respect to descriptor

In the first CUDA kernel (see algorithm 1), the thread associated with atom i calculates the whole descriptor vector \mathbf{q}^i and calls the `__device__` function in Listing 1 to obtain the energy U_i and the derivatives $\partial U_i / \partial q_\nu^i$. The derivatives will be used in the next two CUDA kernels.

Algorithm 1: Pseudo code of the CUDA kernel for evaluating the descriptor vector q_ν^i , the per-atom energy U_i , and the derivatives of the energy with respect the descriptor components $\partial U_i / \partial q_\nu^i$.

```

1 Assign atom  $i$  to CUDA thread  $i$ 
2 if  $i < N$  then
3   Read position  $\mathbf{r}_i$  for atom  $i$  from global memory
4   for  $m = 0$  to  $NN_i^R - 1$  do
5      $j \leftarrow NL_{im}^R$ 
6     Read in  $\mathbf{r}_j$  from global memory and calculate
7      $\mathbf{r}_{ij}$ 
8      $\mathbf{r}_{ij} \leftarrow$  minimum image of  $\mathbf{r}_{ij}$ 
9     Calculate the radial functions  $g_n(r_{ij})$ 
10    according to Eq. (3)
11    Accumulate the radial descriptor components
12    according to Eq. (2)
13  end
14  for  $n = 0$  to  $n_{\max}^A$  do
15    for  $m = 0$  to  $NN_i^A - 1$  do
16       $j \leftarrow NL_{im}^A$ 
17      Read in  $\mathbf{r}_j$  from global memory and
18      calculate  $\mathbf{r}_{ij}$ 
19       $\mathbf{r}_{ij} \leftarrow$  minimum image of  $\mathbf{r}_{ij}$ 
20      Calculate the radial functions  $g_n(r_{ij})$ 
21      according to Eq. (3) but with  $r_c^R$  changed
22      to  $r_c^A$ 
23      Accumulate the summations  $S_{n,k}$ 
24      according to Eq. (12)
25    end
26    Calculate the angular descriptor components
27    for the current  $n$  according to the equations
28    in Sect. II D.
29    Save the summations  $S_{n,k}$  for the current  $n$  to
30    global memory for later use.
31  end
32  Apply the neural network model to get the energy
33   $U_i$  and energy derivatives  $\partial U_i / \partial q_\nu^i$  from the
34  descriptor  $q_\nu^i$  and save them to global memory.
35 end

```

3. Force and virial from the radial descriptor components

In the second CUDA kernel (see [algorithm 2](#)), the thread associated with atom i first calculates the partial forces $\partial U_i / \partial \mathbf{r}_{ij}$ and $\partial U_j / \partial \mathbf{r}_{ji}$ related to the radial descriptor components, and then accumulates the force \mathbf{F}_i and virial \mathbf{W}_i on atom i . For the radial descriptor components, $\partial U_i / \partial \mathbf{r}_{ij}$ and $\partial U_j / \partial \mathbf{r}_{ji}$ only differ a little and it is thus a good choice to calculate both within the CUDA kernel. This algorithm is very similar to that for EAM potentials⁴⁰ (which is an angular-independent many-body potential) as implemented in GPUMD.

Algorithm 2: Pseudo code of the CUDA kernel for evaluating the force and virial from the radial descriptor components.

```

1 Assign atom  $i$  to CUDA thread  $i$ .
2 if  $i < N$  then
3   Read position  $\mathbf{r}_i$  for atom  $i$  from global memory
4   for  $m = 0$  to  $NN_i^R - 1$  do
5      $j \leftarrow NL_{im}^R$ .
6     Read in  $\mathbf{r}_j$  from global memory and calculate
7      $\mathbf{r}_{ij}$ .
8      $\mathbf{r}_{ij} \leftarrow$  minimum image of  $\mathbf{r}_{ij}$ .
9     Calculate the partial force  $\partial U_i / \partial \mathbf{r}_{ij}$  related to
10    the radial descriptor components, i.e., the
11    first term on the right hand side of Eq. (21).
12    Similarly calculate the partial force  $\partial U_j / \partial \mathbf{r}_{ji}$ .
13    Accumulate the force  $\mathbf{F}_i$  on atom  $i$  according
14    to Eq. (22) and Eq. (23).
15    Accumulate the virial  $\mathbf{W}_i$  on atom  $i$  according
16    to Eq. Eq. 24.
17  end
18 end

```

4. Partial forces from the angular descriptor components

Algorithm 3: Pseudo code of the CUDA kernel for evaluating the partial forces $\partial U_i / \partial \mathbf{r}_{ij}$ for all atoms i and all neighbors j of i from the angular descriptor components.

```

1 Assign atom  $i$  to CUDA thread  $i$ 
2 if  $i < N$  then
3   Read position  $\mathbf{r}_i$  for atom  $i$  from global memory
4   for  $m = 0$  to  $NN_i^A - 1$  do
5      $j \leftarrow NL_{im}^A$ 
6     Read in  $\mathbf{r}_j$  from global memory and calculate
7      $\mathbf{r}_{ij}$ 
8      $\mathbf{r}_{ij} \leftarrow$  minimum image of  $\mathbf{r}_{ij}$ 
9     Calculate the partial force  $\partial U_i / \partial \mathbf{r}_{ij}$  related to
10    the angular descriptor components, i.e., the
11    last three terms on the right hand side of
12    Eq. (21).
13     Save the partial force  $\partial U_i / \partial \mathbf{r}_{ij}$  to global
14     memory for later use.
15  end
16 end

```

In the third CUDA kernel (see [algorithm 3](#)), the thread associated with atom i calculates the partial forces $\partial U_i / \partial \mathbf{r}_{ij}$ related to the angular descriptor components and saves them to global memory, which is then used in the next CUDA kernel. For the angular descriptor components, $\partial U_i / \partial \mathbf{r}_{ij}$ and $\partial U_j / \partial \mathbf{r}_{ji}$ differ a lot and it is thus more efficient to use a two-kernel approach: using one CUDA kernel (the current one) to calculate the partial forces $\{\partial U_i / \partial \mathbf{r}_{ij}\}$ for all atom pairs (within the angular cutoff) and save them to global memory, and then using

another CUDA kernel (the next one) to consume them.

5. Force and virial from the angular partial forces

Algorithm 4: Pseudo code of the CUDA kernel for evaluating the force and virial from the angular descriptor components.

```

1 Assign atom  $i$  to CUDA thread  $i$ .
2 if  $i < N$  then
3   Read position  $\mathbf{r}_i$  for atom  $i$  from global memory
4   for  $m = 0$  to  $NN_i^A - 1$  do
5      $j \leftarrow NL_{im}^A$ .
6     Read in  $\mathbf{r}_j$  from global memory and calculate
7      $\mathbf{r}_{ij}$ .
8      $\mathbf{r}_{ij} \leftarrow$  minimum image of  $\mathbf{r}_{ij}$ .
9     Read in the partial force  $\partial U_i / \partial \mathbf{r}_{ij}$  related to
10    the angular descriptor components from
11    global memory.
12   Similarly read in  $U_j / \partial \mathbf{r}_{ji}$  from global memory
13   with some index manipulations.
14   Accumulate the force  $\mathbf{F}_i$  on atom  $i$  according
15   to Eq. (22) and Eq. (23).
16   Accumulate the virial  $\mathbf{W}_i$  on atom  $i$  according
17   to Eq. (24).
18 end
19 end

```

After obtaining the partial force $\{\partial U_i / \partial \mathbf{r}_{ij}\}$ related to the angular descriptor components, we use a CUDA kernel (see [algorithm 4](#)) to accumulate the corresponding force and virial. In this kernel, we load the partial force $\partial U_i / \partial \mathbf{r}_{ij}$ and $\partial U_j / \partial \mathbf{r}_{ji}$, which are related to each other by an exchange of atom indices i and j . Then we accumulate the force \mathbf{F}_i on atom i according to Eqs. (22) and (23), and accumulate the virial \mathbf{W}_i on atom i according to Eq. (24). This is a general CUDA kernel used in the GPUMD package for all the angular-dependent many-body potentials, such as the Stillinger-Weber⁷³ and Tersoff potentials.³⁸

REFERENCES

- 1 J. Behler, “Perspective: Machine learning potentials for atomistic simulations,” *The Journal of Chemical Physics* **145**, 170901 (2016).
- 2 V. L. Deringer, M. A. Caro, and G. Csányi, “Machine Learning Interatomic Potentials as Emerging Tools for Materials Science,” *Advanced Materials* **31**, 1902765 (2019).
- 3 T. Mueller, A. Hernandez, and C. Wang, “Machine learning for interatomic potential models,” *The Journal of Chemical Physics* **152**, 050902 (2020).
- 4 F. Noé, A. Tkatchenko, K.-R. Müller, and C. Clementi, “Machine Learning for Molecular

Simulation,” *Annual Review of Physical Chemistry* **71**, 361–390 (2020).

- 5 A. M. Miksch, T. Morawietz, J. Kästner, A. Urban, and N. Artrith, “Strategies for the construction of machine-learning potentials for accurate and efficient atomic-scale simulations,” *Machine Learning: Science and Technology* **2**, 031001 (2021).
- 6 Y. Mishin, “Machine-learning interatomic potentials for materials science,” *Acta Materialia* **214**, 116980 (2021).
- 7 O. T. Unke, S. Chmiela, H. E. Sauceda, M. Gastegger, I. Poltavsky, K. T. Schütt, A. Tkatchenko, and K.-R. Müller, “Machine Learning Force Fields,” *Chemical Reviews* **121**, 10142–10186 (2021).
- 8 A. P. Bartók, M. C. Payne, R. Kondor, and G. Csányi, “Gaussian Approximation Potentials: The Accuracy of Quantum Mechanics, without the Electrons,” *Phys. Rev. Lett.* **104**, 136403 (2010).
- 9 A. P. Bartók, R. Kondor, and G. Csányi, “On representing chemical environments,” *Phys. Rev. B* **87**, 184115 (2013).
- 10 V. L. Deringer and G. Csányi, “Machine learning based interatomic potential for amorphous carbon,” *Phys. Rev. B* **95**, 094203 (2017).
- 11 A. Thompson, L. Swiler, C. Trott, S. Foiles, and G. Tucker, “Spectral neighbor analysis method for automated generation of quantum-accurate interatomic potentials,” *Journal of Computational Physics* **285**, 316–330 (2015).
- 12 A. Khorshidi and A. A. Peterson, “Amp: A modular approach to machine learning in atomistic simulations,” *Computer Physics Communications* **207**, 310–324 (2016).
- 13 N. Artrith and A. Urban, “An implementation of artificial neural-network potentials for atomistic materials simulations: Performance for TiO₂,” *Computational Materials Science* **114**, 135–150 (2016).
- 14 N. Artrith, A. Urban, and G. Ceder, “Efficient and accurate machine-learning interpolation of atomic energies in compositions with many species,” *Phys. Rev. B* **96**, 014112 (2017).
- 15 J. S. Smith, O. Isayev, and A. E. Roitberg, “ANI-1: an extensible neural network potential with DFT accuracy at force field computational cost,” *Chem. Sci.* **8**, 3192–3203 (2017).
- 16 K. T. Schütt, H. E. Sauceda, P.-J. Kindermans, A. Tkatchenko, and K.-R. Müller, “SchNet—A deep learning architecture for molecules and materials,” *The Journal of Chemical Physics* **148**, 241722 (2018).
- 17 H. Wang, L. Zhang, J. Han, and W. E, “DeePMD-kit: A deep learning package for many-body potential energy representation and molecular dynamics,” *Computer Physics Communications* **228**, 178–184 (2018).
- 18 L. Zhang, J. Han, H. Wang, R. Car, and W. E, “Deep Potential Molecular Dynamics: A Scalable Model with the Accuracy of Quantum Mechanics,” *Phys. Rev. Lett.* **120**, 143001 (2018).
- 19 L. Zhang, J. Han, H. Wang, W. A. Saidi, R. Car, and

W. E, "End-to-end symmetry preserving inter-atomic potential energy model for finite and extended systems," (2018), [arXiv:1805.09003 \[physics.comp-ph\]](https://arxiv.org/abs/1805.09003).

²⁰K. Yao, J. E. Herr, D. Toth, R. Mckintyre, and J. Parkhill, "The TensorMol-0.1 model chemistry: a neural network augmented with long-range physics," *Chem. Sci.* **9**, 2261–2269 (2018).

²¹O. T. Unke and M. Meuwly, "PhysNet: A Neural Network for Predicting Energies, Forces, Dipole Moments, and Partial Charges," *Journal of Chemical Theory and Computation* **15**, 3678–3693 (2019).

²²C. Chen, W. Ye, Y. Zuo, C. Zheng, and S. P. Ong, "Graph Networks as a Universal Machine Learning Framework for Molecules and Crystals," *Chemistry of Materials* **31**, 3564–3572 (2019).

²³M. A. Caro, "Optimizing many-body atomic descriptors for enhanced computational performance of machine learning based interatomic potentials," *Phys. Rev. B* **100**, 024112 (2019).

²⁴S. Chmiela, H. E. Sauceda, I. Poltavsky, K.-R. Müller, and A. Tkatchenko, "sGDML: Constructing accurate and data efficient molecular force fields using machine learning," *Computer Physics Communications* **240**, 38–45 (2019).

²⁵A. Singraber, J. Behler, and C. Dellago, "Library-Based LAMMPS Implementation of High-Dimensional Neural Network Potentials," *Journal of Chemical Theory and Computation* **15**, 1827–1840 (2019).

²⁶K. Lee, D. Yoo, W. Jeong, and S. Han, "SIMPLE-NN: An efficient package for training and executing neural-network interatomic potentials," *Computer Physics Communications* **242**, 95–103 (2019).

²⁷R. Lot, F. Pellegrini, Y. Shaidu, and E. Küçükbenli, "PANNA: Properties from Artificial Neural Network Architectures," *Computer Physics Communications* **256**, 107402 (2020).

²⁸A. S. Christensen, L. A. Bratholm, F. A. Faber, and O. Anatole von Lilienfeld, "FCHL revisited: Faster and more accurate quantum machine learning," *The Journal of Chemical Physics* **152**, 044107 (2020).

²⁹Y. Shao, M. Hellström, P. D. Mitev, L. Knijff, and C. Zhang, "PiNN: A Python Library for Building Atomic Neural Networks of Molecules and Materials," *Journal of Chemical Information and Modeling* **60**, 1184–1193 (2020).

³⁰A. V. Shapeev, "Moment Tensor Potentials: A Class of Systematically Improvable Interatomic Potentials," *Multiscale Modeling & Simulation* **14**, 1153–1173 (2016).

³¹I. S. Novikov, K. Gubaev, E. V. Podryabinkin, and A. V. Shapeev, "The MLIP package: moment tensor potentials with MPI and active learning," *Machine Learning: Science and Technology* **2**, 025002 (2021).

³²Y. Zhang, J. Xia, and B. Jiang, "Reann: A pytorch-based end-to-end multi-functional deep neural network package for molecular, reactive, and periodic systems," *The Journal of Chemical Physics* **156**, 114801 (2022).

³³J. Byggmästar, K. Nordlund, and F. Djurabekova, "Modeling refractory high-entropy alloys with efficient machine-learned interatomic potentials: Defects and segregation," *Phys. Rev. B* **104**, 104101 (2021).

³⁴H. Yanxon, D. Zagaceta, B. Tang, D. S. Matteson, and Q. Zhu, "PyXtal_FF: a python library for automated force field generation," *Machine Learning: Science and Technology* **2**, 027001 (2021).

³⁵Y. Lysogorskiy, C. v. d. Oord, A. Bochkarev, S. Menon, M. Rinaldi, T. Hammerschmidt, M. Mrovec, A. Thompson, G. Csányi, C. Ortner, *et al.*, "Performant implementation of the atomic cluster expansion (PACE) and application to copper and silicon," *npj Computational Materials* **7**, 1–12 (2021).

³⁶A. Bochkarev, Y. Lysogorskiy, S. Menon, M. Qamar, M. Mrovec, and R. Drautz, "Efficient parametrization of the atomic cluster expansion," *Phys. Rev. Materials* **6**, 013804 (2022).

³⁷M. Wen, Y. Afshar, R. S. Elliott, and E. B. Tadmor, "KLIFF: A framework to develop physics-based and machine learning interatomic potentials," *Computer Physics Communications* **272**, 108218 (2022).

³⁸J. Tersoff, "Modeling solid-state chemistry: Interatomic potentials for multicomponent systems," *Phys. Rev. B* **39**, 5566–5568 (1989).

³⁹W. Jia, H. Wang, M. Chen, D. Lu, L. Lin, R. Car, W. E, and L. Zhang, "Pushing the Limit of Molecular Dynamics with Ab Initio Accuracy to 100 Million Atoms with Machine Learning," in *Proceedings of the International Conference for High Performance Computing, Networking, Storage and Analysis, SC '20* (IEEE Press, 2020).

⁴⁰M. S. Daw and M. I. Baskes, "Embedded-atom method: Derivation and application to impurities, surfaces, and other defects in metals," *Phys. Rev. B* **29**, 6443–6453 (1984).

⁴¹Z. Fan, Z. Zeng, C. Zhang, Y. Wang, K. Song, H. Dong, Y. Chen, and T. Ala-Nissila, "Neuroevolution machine learning potentials: Combining high accuracy and low cost in atomistic simulations and application to heat transport," *Phys. Rev. B* **104**, 104309 (2021).

⁴²Z. Fan, "Improving the accuracy of the neuroevolution machine learning potential for multi-component systems," *Journal of Physics: Condensed Matter* **34**, 125902 (2022).

⁴³Z. Fan, T. Siro, and A. Harju, "Accelerated molecular dynamics force evaluation on graphics processing units for thermal conductivity calculations," *Computer Physics Communications* **184**, 1414–1425 (2013).

⁴⁴Z. Fan, W. Chen, V. Vierimaa, and A. Harju, "Efficient molecular dynamics simulations with many-body potentials on graphics processing units," *Computer Physics Communications* **218**, 10 – 16 (2017).

⁴⁵Y. Zhang, J. Xia, and B. Jiang, "Physically Motivated

Recursively Embedded Atom Neural Networks: Incorporating Local Completeness and Nonlocality,” *Phys. Rev. Lett.* **127**, 156002 (2021).

⁴⁶R. Drautz, “Atomic cluster expansion for accurate and transferable interatomic potentials,” *Phys. Rev. B* **99**, 014104 (2019).

⁴⁷D. P. Kovács, C. v. d. Oord, J. Kucera, A. E. A. Allen, D. J. Cole, C. Ortner, and G. Csányi, “Linear Atomic Cluster Expansion Force Fields for Organic Molecules: Beyond RMSE,” *Journal of Chemical Theory and Computation* **17**, 7696–7711 (2021).

⁴⁸G. Dusson, M. Bachmayr, G. Csányi, R. Drautz, S. Ettner, C. van der Oord, and C. Ortner, “Atomic cluster expansion: Completeness, efficiency and stability,” *Journal of Computational Physics* **454**, 110946 (2022).

⁴⁹J. Behler and M. Parrinello, “Generalized Neural-Network Representation of High-Dimensional Potential-Energy Surfaces,” *Phys. Rev. Lett.* **98**, 146401 (2007).

⁵⁰Musil, Felix and Grisafi, Andrea and Bartók, Albert P. and Ortner, Christoph and Csányi, Gábor and Ceriotti, Michele, “Physics-inspired structural representations for molecules and materials,” *Chemical Reviews* **121**, 9759–9815 (2021).

⁵¹M. F. Langer, A. Goeßmann, and M. Rupp, “Representations of molecules and materials for interpolation of quantum-mechanical simulations via machine learning,” *npj Computational Materials* **8**, 41 (2022).

⁵²M. Gastegger, L. Schwiedrzik, M. Bittermann, F. Berzsényi, and P. Marquetand, “wACSF—Weighted atom-centered symmetry functions as descriptors in machine learning potentials,” *The Journal of Chemical Physics* **148**, 241709 (2018).

⁵³Nigam, Jigyasa and Pozdnyakov, Sergey and Fraux, Guillaume and Ceriotti, Michele, “Unified theory of atom-centered representations and message-passing machine-learning schemes,” *The Journal of Chemical Physics* **0**, null (0).

⁵⁴B. Parsaeifard and S. Goedecker, “Manifolds of quasi-constant SOAP and ACSF fingerprints and the resulting failure to machine learn four-body interactions,” *The Journal of Chemical Physics* **156**, 034302 (2022).

⁵⁵S. N. Pozdnyakov, M. J. Willatt, A. P. Bartók, C. Ortner, G. Csányi, and M. Ceriotti, “Incompleteness of Atomic Structure Representations,” *Phys. Rev. Lett.* **125**, 166001 (2020).

⁵⁶A. Glielmo, C. Zeni, and A. De Vita, “Efficient non-parametric n -body force fields from machine learning,” *Phys. Rev. B* **97**, 184307 (2018).

⁵⁷M. J. Willatt, F. Musil, and M. Ceriotti, “Atom-density representations for machine learning,” *The Journal of Chemical Physics* **150**, 154110 (2019).

⁵⁸M. Uhrin, “Through the eyes of a descriptor: Constructing complete, invertible descriptions of atomic environments,” *Phys. Rev. B* **104**, 144110 (2021).

⁵⁹A. Stone and C. Wood, “Root-rational-fraction package for exact calculation of vector-coupling coefficients,” *Computer Physics Communications* **21**, 195–205 (1980).

⁶⁰Z. Fan, L. F. C. Pereira, H.-Q. Wang, J.-C. Zheng, D. Donadio, and A. Harju, “Force and heat current formulas for many-body potentials in molecular dynamics simulations with applications to thermal conductivity calculations,” *Phys. Rev. B* **92**, 094301 (2015).

⁶¹A. J. Gabourie, Z. Fan, T. Ala-Nissila, and E. Pop, “Spectral decomposition of thermal conductivity: Comparing velocity decomposition methods in homogeneous molecular dynamics simulations,” *Phys. Rev. B* **103**, 205421 (2021).

⁶²M. Gill-Comeau and L. J. Lewis, “Heat conductivity in graphene and related materials: A time-domain modal analysis,” *Phys. Rev. B* **92**, 195404 (2015).

⁶³Z. Fan, L. F. C. Pereira, P. Hirvonen, M. M. Ervasti, K. R. Elder, D. Donadio, T. Ala-Nissila, and A. Harju, “Thermal conductivity decomposition in two-dimensional materials: Application to graphene,” *Phys. Rev. B* **95**, 144309 (2017).

⁶⁴K. Xu, Z. Fan, J. Zhang, N. Wei, and T. Ala-Nissila, “Thermal transport properties of single-layer black phosphorus from extensive molecular dynamics simulations,” *Modelling and Simulation in Materials Science and Engineering* **26**, 085001 (2018).

⁶⁵J. Brorsson, A. Hashemi, Z. Fan, E. Fransson, F. Eriksson, T. Ala-Nissila, A. V. Krasheninnikov, H.-P. Komsa, and P. Erhart, “Efficient Calculation of the Lattice Thermal Conductivity by Atomistic Simulations with Ab Initio Accuracy,” *Advanced Theory and Simulations* **5**, 2100217 (2022).

⁶⁶C. Verdi, F. Karsai, P. Liu, R. Jinnouchi, and G. Kresse, “Thermal transport and phase transitions of zirconia by on-the-fly machine-learned interatomic potentials,” *npj Computational Materials* **7**, 1–9 (2021).

⁶⁷P. Boone, H. Babaei, and C. E. Wilmer, “Heat Flux for Many-Body Interactions: Corrections to LAMMPS,” *Journal of Chemical Theory and Computation* **15**, 5579–5587 (2019).

⁶⁸T. Schaul, T. Glasmachers, and J. Schmidhuber, “High Dimensions and Heavy Tails for Natural Evolution Strategies,” in *Proceedings of the 13th Annual Conference on Genetic and Evolutionary Computation*, GECCO ’11 (Association for Computing Machinery, New York, NY, USA, 2011) pp. 845–852.

⁶⁹J. A. Anderson, C. D. Lorenz, and A. Traverset, “General purpose molecular dynamics simulations fully implemented on graphics processing units,” *Journal of Computational Physics* **227**, 5342–5359 (2008).

⁷⁰S. Páll, A. Zhmurov, P. Bauer, M. Abraham, M. Lundborg, A. Gray, B. Hess, and E. Lindahl, “Heterogeneous parallelization and acceleration of molecular dynamics simulations in GROMACS,” *The Journal of Chemical Physics* **153**, 134110 (2020).

⁷¹A. P. Thompson, H. M. Aktulga, R. Berger, D. S. Bolintineanu, W. M. Brown, P. S. Crozier, P. J. in ’t Veld, A. Kohlmeyer, S. G. Moore, T. D. Nguyen,

R. Shan, M. J. Stevens, J. Tranchida, C. Trott, and S. J. Plimpton, "LAMMPS - a flexible simulation tool for particle-based materials modeling at the atomic, meso, and continuum scales," *Computer Physics Communications* **271**, 108171 (2022).

⁷²Z. Fan, Y. Wang, X. Gu, P. Qian, Y. Su, and T. Ala-Nissila, "A minimal Tersoff potential for diamond silicon with improved descriptions of elastic and phonon transport properties," *Journal of Physics: Condensed Matter* **32**, 135901 (2019).

⁷³F. H. Stillinger and T. A. Weber, "Computer simulation of local order in condensed phases of silicon," *Phys. Rev. B* **31**, 5262–5271 (1985).

⁷⁴F. Eriksson, E. Fransson, and P. Erhart, "The Hiphive Package for the Extraction of High-Order Force Constants by Machine Learning," *Advanced Theory and Simulations* **2**, 1800184 (2019).

⁷⁵H. J. C. Berendsen, J. P. M. Postma, W. F. van Gunsteren, A. DiNola, and J. R. Haak, "Molecular dynamics with coupling to an external bath," *The Journal of Chemical Physics* **81**, 3684–3690 (1984).

⁷⁶S. Nosé, "A unified formulation of the constant temperature molecular dynamics methods," *The Journal of Chemical Physics* **81**, 511–519 (1984).

⁷⁷W. G. Hoover, "Canonical dynamics: Equilibrium phase-space distributions," *Phys. Rev. A* **31**, 1695–1697 (1985).

⁷⁸G. J. Martyna, M. L. Klein, and M. Tuckerman, "Nosé-Hoover chains: The canonical ensemble via continuous dynamics," *The Journal of Chemical Physics* **97**, 2635–2643 (1992).

⁷⁹G. Bussi, D. Donadio, and M. Parrinello, "Canonical sampling through velocity rescaling," *The Journal of Chemical Physics* **126**, 014101 (2007).

⁸⁰G. Bussi and M. Parrinello, "Accurate sampling using Langevin dynamics," *Phys. Rev. E* **75**, 056707 (2007).

⁸¹B. Leimkuhler and C. Matthews, "Robust and efficient configurational molecular sampling via Langevin dynamics," *The Journal of Chemical Physics* **138**, 174102 (2013).

⁸²M. Bernetti and G. Bussi, "Pressure control using stochastic cell rescaling," *The Journal of Chemical Physics* **153**, 114107 (2020).

⁸³M. S. Green, "Markoff Random Processes and the Statistical Mechanics of Time-dependent Phenomena. II. Irreversible Processes in Fluids," *The Journal of Chemical Physics* **22**, 398–413 (1954).

⁸⁴R. Kubo, "Statistical-Mechanical Theory of Irreversible Processes. I. General Theory and Simple Applications to Magnetic and Conduction Problems," *Journal of the Physical Society of Japan* **12**, 570–586 (1957).

⁸⁵Z. Li, S. Xiong, C. Sievers, Y. Hu, Z. Fan, N. Wei, H. Bao, S. Chen, D. Donadio, and T. Ala-Nissila, "Influence of thermostatting on nonequilibrium molecular dynamics simulations of heat conduction in solids," *The Journal of Chemical Physics* **151**, 234105 (2019).

⁸⁶D. J. Evans, "Homogeneous NEMD algorithm for thermal conductivity—Application of non-canonical linear response theory," *Physics Letters A* **91**, 457 – 460 (1982).

⁸⁷Z. Fan, H. Dong, A. Harju, and T. Ala-Nissila, "Homogeneous nonequilibrium molecular dynamics method for heat transport and spectral decomposition with many-body potentials," *Phys. Rev. B* **99**, 064308 (2019).

⁸⁸H. Dong, Z. Fan, L. Shi, A. Harju, and T. Ala-Nissila, "Equivalence of the equilibrium and the nonequilibrium molecular dynamics methods for thermal conductivity calculations: From bulk to nanowire silicon," *Physical Review B* **97**, 094305 (2018).

⁸⁹B. Mortazavi, Z. Fan, L. F. C. Pereira, A. Harju, and T. Rabczuk, "Amorphized graphene: A stiff material with low thermal conductivity," *Carbon* **103**, 318–326 (2016).

⁹⁰K. Azizi, P. Hirvonen, Z. Fan, A. Harju, K. R. Elder, T. Ala-Nissila, and S. M. V. Allaei, "Kapitza thermal resistance across individual grain boundaries in graphene," *Carbon* **125**, 384 – 390 (2017).

⁹¹Z. Fan, P. Hirvonen, L. F. C. Pereira, M. M. Ervasti, K. R. Elder, D. Donadio, A. Harju, and T. Ala-Nissila, "Bimodal Grain-Size Scaling of Thermal Transport in Polycrystalline Graphene from Large-Scale Molecular Dynamics Simulations," *Nano Letters* **17**, 5919–5924 (2017).

⁹²B. Mortazavi, A. Lherbier, Z. Fan, A. Harju, T. Rabczuk, and J.-C. Charlier, "Thermal and electronic transport characteristics of highly stretchable graphene kirigami," *Nanoscale* **9**, 16329–16341 (2017).

⁹³B. Mortazavi, M. Makaremi, M. Shahrokh, Z. Fan, and T. Rabczuk, "N-graphdiyne two-dimensional nanomaterials: Semiconductors with low thermal conductivity and high stretchability," *Carbon* **137**, 57–67 (2018).

⁹⁴H. Dong, P. Hirvonen, Z. Fan, and T. Ala-Nissila, "Heat transport in pristine and polycrystalline single-layer hexagonal boron nitride," *Phys. Chem. Chem. Phys.* **20**, 24602–24612 (2018).

⁹⁵K. Xu, A. J. Gabourie, A. Hashemi, Z. Fan, N. Wei, A. B. Farimani, H.-P. Komsa, A. V. Krasheninnikov, E. Pop, and T. Ala-Nissila, "Thermal transport in MoS₂ from molecular dynamics using different empirical potentials," *Phys. Rev. B* **99**, 054303 (2019).

⁹⁶X. Gu, Z. Fan, H. Bao, and C. Y. Zhao, "Revisiting phonon-phonon scattering in single-layer graphene," *Phys. Rev. B* **100**, 064306 (2019).

⁹⁷X. Wu and Q. Han, "Thermal conductivity of monolayer hexagonal boron nitride: From defective to amorphous," *Computational Materials Science* **184**, 109938 (2020).

⁹⁸X. Wu and Q. Han, "Thermal conductivity of defective graphene: an efficient molecular dynamics study based on graphics processing units," *Nanotechnology* **31**, 215708 (2020).

⁹⁹X. Wu and Q. Han, "Semidefective Graphene/h-BN In-Plane Heterostructures: Enhancing Interface Ther-

mal Conductance by Topological Defects," *The Journal of Physical Chemistry C* **125**, 2748–2760 (2021).

¹⁰⁰X. Wu and Q. Han, "Thermal transport in pristine and defective two-dimensional polyaniline (C3N)," *International Journal of Heat and Mass Transfer* **173**, 121235 (2021).

¹⁰¹H. Dong, P. Hirvonen, Z. Fan, P. Qian, Y. Su, and T. Ala-Nissila, "Heat transport across graphene/hexagonal-BN tilted grain boundaries from phase-field crystal model and molecular dynamics simulations," *Journal of Applied Physics* **130**, 235102 (2021).

¹⁰²P. Ying, T. Liang, Y. Du, J. Zhang, X. Zeng, and Z. Zhong, "Thermal transport in planar sp₂-hybridized carbon allotropes: A comparative study of biphenylene network, pentaheptite and graphene," *International Journal of Heat and Mass Transfer* **183**, 122060 (2022).

¹⁰³W. Sha and F. Guo, "Thermal transport in two-dimensional carbon nitrides: A comparative molecular dynamics study," *Carbon Trends* **7**, 100161 (2022).

¹⁰⁴A. Rajabpour, Z. Fan, and S. M. Vaez Allaei, "Inter-layer and intra-layer heat transfer in bilayer/monolayer graphene van der Waals heterostructure: Is there a Kapitza resistance analogous?" *Applied Physics Letters* **112**, 233104 (2018).

¹⁰⁵A. J. Gabourie, S. V. Suryavanshi, A. B. Farimani, and E. Pop, "Reduced thermal conductivity of supported and encased monolayer and bilayer MoS₂," *2D Materials* **8**, 011001 (2020).

¹⁰⁶S. E. Kim, F. Mujid, A. Rai, F. Eriksson, J. Suh, P. Poddar, A. Ray, C. Park, E. Fransson, Y. Zhong, D. A. Muller, P. Erhart, D. G. Cahill, and J. Park, "Extremely anisotropic van der Waals thermal conductors," *Nature* **597**, 660–665 (2021).

¹⁰⁷X. Wu and Q. Han, "Phonon Thermal Transport across Multilayer Graphene/Hexagonal Boron Nitride van der Waals Heterostructures," *ACS Applied Materials & Interfaces* **13**, 32564–32578 (2021).

¹⁰⁸X. Wu and Q. Han, "Transition from incoherent to coherent phonon thermal transport across graphene/h-BN van der Waals superlattices," *International Journal of Heat and Mass Transfer* **184**, 122390 (2022).

¹⁰⁹X. Wu and Q. Han, "Maximum thermal conductivity of multilayer graphene with periodic two-dimensional empty space," *International Journal of Heat and Mass Transfer* **191**, 122829 (2022).

¹¹⁰H. Feng, K. Zhang, X. Wang, G. Zhang, and X. Guo, "Thermal transport of bilayer graphene: a homogeneous nonequilibrium molecular dynamics study," *Physica Scripta* **97**, 045704 (2022).

¹¹¹H. Dong, Z. Fan, P. Qian, T. Ala-Nissila, and Y. Su, "Thermal conductivity reduction in carbon nanotube by fullerene encapsulation: A molecular dynamics study," *Carbon* **161**, 800–808 (2020).

¹¹²G. Barbalinardo, Z. Chen, H. Dong, Z. Fan, and D. Donadio, "Ultrahigh Convergent Thermal Conductivity of Carbon Nanotubes from Comprehensive Atomistic Modeling," *Phys. Rev. Lett.* **127**, 025902 (2021).

¹¹³T. Liang, K. Xu, M. Han, Y. Yao, Z. Zhang, X. Zeng, J. Xu, and J. Wu, "Abnormally High Thermal Conductivity in Fivefold Twinned Diamond Nanowires," *Materials Today Physics* **100705** (2022).

¹¹⁴L. Isaeva, G. Barbalinardo, D. Donadio, and S. Baroni, "Modeling heat transport in crystals and glasses from a unified lattice-dynamical approach," *Nature Communications* **10**, 3853 (2019).

¹¹⁵B. Fu, K. D. Parrish, H.-Y. Kim, G. Tang, and A. J. H. McGaughey, "Phonon confinement and transport in ultrathin films," *Phys. Rev. B* **101**, 045417 (2020).

¹¹⁶Z. Zhang, Y. Guo, M. Bescond, J. Chen, M. Nomura, and S. Volz, "Generalized decay law for particlelike and wavelike thermal phonons," *Phys. Rev. B* **103**, 184307 (2021).

¹¹⁷H. Wang, Y. Cheng, Z. Fan, Y. Guo, Z. Zhang, M. Bescond, M. Nomura, T. Ala-Nissila, S. Volz, and S. Xiong, "Anomalous thermal conductivity enhancement in low dimensional resonant nanostructures due to imperfections," *Nanoscale* **13**, 10010–10015 (2021).

¹¹⁸H. Dong, S. Xiong, Z. Fan, P. Qian, Y. Su, and T. Ala-Nissila, "Interpretation of apparent thermal conductivity in finite systems from equilibrium molecular dynamics simulations," *Phys. Rev. B* **103**, 035417 (2021).

¹¹⁹N. W. Lundgren, G. Barbalinardo, and D. Donadio, "Mode localization and suppressed heat transport in amorphous alloys," *Phys. Rev. B* **103**, 024204 (2021).

¹²⁰K. Li, Y. Cheng, H. Wang, Y. Guo, Z. Zhang, M. Bescond, M. Nomura, S. Volz, X. Zhang, and S. Xiong, "Phonon resonant effect in silicon membranes with different crystallographic orientations," *International Journal of Heat and Mass Transfer* **183**, 122144 (2022).

¹²¹S. Jin, Z. Zhang, Y. Guo, J. Chen, M. Nomura, and S. Volz, "Optimization of interfacial thermal transport in Si/Ge heterostructure driven by machine learning," *International Journal of Heat and Mass Transfer* **182**, 122014 (2022).

¹²²W. Jiang, Y. Zhang, L. Zhang, and H. Wang, "Accurate Deep Potential model for the Al-Cu-Mg alloy in the full concentration space," *Chinese Physics B* **30**, 050706 (2021).

¹²³A. P. Bartók, J. Kermode, N. Bernstein, and G. Csányi, "Machine Learning a General-Purpose Interatomic Potential for Silicon," *Phys. Rev. X* **8**, 041048 (2018).

¹²⁴J. Nigam, S. Pozdnyakov, and M. Ceriotti, "Recursive evaluation and iterative contraction of N-body equivariant features," *The Journal of Chemical Physics* **153**, 121101 (2020).

¹²⁵S. Chmiela, A. Tkatchenko, H. E. Sauceda, I. Poltavsky, K. T. Schütt, and K.-R. Müller, "Machine learning of accurate energy-conserving molecular force fields," *Science Advances* **3**, e1603015 (2017).

¹²⁶A. S. Christensen and O. A. von Lilienfeld, "On the

role of gradients for machine learning of molecular energies and forces,” *Machine Learning: Science and Technology* **1**, 045018 (2020).

¹²⁷M. Gastegger, J. Behler, and P. Marquetand, “Machine learning molecular dynamics for the simulation of infrared spectra,” *Chem. Sci.* **8**, 6924–6935 (2017).

¹²⁸J. S. Smith, B. Nebgen, N. Lubbers, O. Isayev, and A. E. Roitberg, “Less is more: Sampling chemical space with active learning,” *The Journal of Chemical Physics* **148**, 241733 (2018).

¹²⁹L. Zhang, D.-Y. Lin, H. Wang, R. Car, and W. E, “Active learning of uniformly accurate interatomic potentials for materials simulation,” *Phys. Rev. Materials* **3**, 023804 (2019).

¹³⁰M. Wen and E. B. Tadmor, “Uncertainty quantification in molecular simulations with dropout neural network potentials,” *npj Computational Materials* **6**, 1–10 (2020).

¹³¹C. Schran, J. Behler, and D. Marx, “Automated Fitting of Neural Network Potentials at Coupled Cluster Accuracy: Protonated Water Clusters as Testing Ground,” *Journal of Chemical Theory and Computation* **16**, 88–99 (2020).

¹³²M. Karabin and D. Perez, “An entropy-maximization approach to automated training set generation for interatomic potentials,” *The Journal of Chemical Physics* **153**, 094110 (2020).

¹³³E. V. Podryabinkin and A. V. Shapeev, “Active learning of linearly parametrized interatomic potentials,” *Computational Materials Science* **140**, 171–180 (2017).

¹³⁴V. Zaverkin and J. Kästner, “Exploration of transferable and uniformly accurate neural network interatomic potentials using optimal experimental design,” *Machine Learning: Science and Technology* **2**, 035009 (2021).

¹³⁵J. P. Janet, C. Duan, T. Yang, A. Nandy, and H. J. Kulik, “A quantitative uncertainty metric controls error in neural network-driven chemical discovery,” *Chemical Science* **10**, 7913–7922 (2019).

¹³⁶K. Shimamura, Y. Takeshita, S. Fukushima, A. Koura, and F. Shimojo, “Computational and training requirements for interatomic potential based on artificial neural network for estimating low thermal conductivity of silver chalcogenides,” *The Journal of Chemical Physics* **153**, 234301 (2020).

¹³⁷M. A. Caro, V. L. Deringer, J. Koskinen, T. Laurila, and G. Csányi, “Growth Mechanism and Origin of High sp^3 Content in Tetrahedral Amorphous Carbon,” *Phys. Rev. Lett.* **120**, 166101 (2018).

¹³⁸Wang, Yanzhou and Fan, Zheyong and Qian, Ping and Ala-Nissila, Tapio and Caro, Miguel A., “Structure and pore size distribution in nanoporous carbon,” *Chemistry of Materials* **34**, 617–628 (2022).

¹³⁹J. M. Dickey and A. Paskin, “Computer Simulation of the Lattice Dynamics of Solids,” *Phys. Rev.* **188**, 1407–1418 (1969).

¹⁴⁰J. M. Haile, *Molecular Dynamics Simulation: Elementary Methods* (John Wiley & Sons, Inc, 1992).

¹⁴¹X. Gu, Z. Fan, and H. Bao, “Thermal conductivity prediction by atomistic simulation methods: Recent advances and detailed comparison,” *Journal of Applied Physics* **130**, 210902 (2021).

¹⁴²A. H. Larsen, J. J. Mortensen, J. Blomqvist, I. E. Castelli, R. Christensen, M. Dulak, J. Friis, M. N. Groves, B. Hammer, C. Hargus, E. D. Hermes, P. C. Jennings, P. B. Jensen, J. Kermode, J. R. Kitchin, E. L. Kolsbørg, J. Kubal, K. Kaasbørg, S. Lysgaard, J. B. Maronsson, T. Maxson, T. Olsen, L. Pastewka, A. Peterson, C. Rostgaard, J. Schiøtz, O. Schütt, M. Strange, K. S. Thygesen, T. Vegge, L. Vilhelmsen, M. Walter, Z. Zeng, and K. W. Jacobsen, “The atomic simulation environment—a Python library for working with atoms,” *Journal of Physics: Condensed Matter* **29**, 273002 (2017).

¹⁴³Z. Fan, “GPUMD: A package for constructing accurate machine-learned potentials and performing highly efficient atomistic simulations,” [10.5281/zenodo.6548090](https://doi.org/10.5281/zenodo.6548090) (2022).